NASA/TM–20260002074

A Hybrid RANS-LES Methodology for the Prediction of Turbulent Separated Flows

Ali Uzun
Analytical Mechanics Associates, Hampton, Virginia

Mujeeb R. Malik
Langley Research Center, Hampton, Virginia

March 2026

NASA STI Program Report Series

Since its founding, NASA has been dedicated to the advancement of aeronautics and space science. The NASA scientific and technical information (STI) program plays a key part in helping NASA maintain this important role.

The NASA STI program operates under the auspices of the Agency Chief Information Officer. It collects, organizes, provides for archiving, and disseminates NASA's STI. The NASA STI program provides access to the NTRS Registered and its public interface, the NASA Technical Reports Server, thus providing one of the largest collections of aeronautical and space science STI in the world. Results are published in both non-NASA channels and by NASA in the NASA STI Report Series, which includes the following report types:

- TECHNICAL PUBLICATION. Reports of completed research or a major significant phase of research that present the results of NASA Programs and include extensive data or theoretical analysis. Includes compilations of significant scientific and technical data and information deemed to be of continuing reference value. NASA counterpart of peer-reviewed formal professional papers but has less stringent limitations on manuscript length and extent of graphic presentations.

- TECHNICAL MEMORANDUM. Scientific and technical findings that are preliminary or of specialized interest, e.g., quick release reports, working papers, and bibliographies that contain minimal annotation. Does not contain extensive analysis.

- CONTRACTOR REPORT. Scientific and technical findings by NASA-sponsored contractors and grantees.

- CONFERENCE PUBLICATION. Collected papers from scientific and technical conferences, symposia, seminars, or other meetings sponsored or co-sponsored by NASA.

- SPECIAL PUBLICATION. Scientific, technical, or historical information from NASA programs, projects, and missions, often concerned with subjects having substantial public interest.

- TECHNICAL TRANSLATION. English-language translations of foreign scientific and technical material pertinent to NASA's mission.

Specialized services also include organizing and publishing research results, distributing specialized research announcements and feeds, providing information desk and personal search support, and enabling data exchange services.

For more information about the NASA STI program, see the following:

- Access the NASA STI program home page at http://www.sti.nasa.gov

NASA/TM–20260002074

A Hybrid RANS-LES Methodology for the Prediction of Turbulent Separated Flows

Ali Uzun
Analytical Mechanics Associates, Hampton, Virginia

Mujeeb R. Malik
Langley Research Center, Hampton, Virginia

National Aeronautics and
Space Administration

Langley Research Center
Hampton, Virginia 23681-2199

March 2026

Available from:

NASA STI Program / Mail Stop 050
NASA Langley Research Center
Hampton, VA 23681-2199

A Hybrid RANS-LES Methodology for the Prediction of Turbulent Separated Flows

Ali Uzun
Analytical Mechanics Associates, Hampton, Virginia 23666

Mujeeb R. Malik
NASA Langley Research Center, Hampton, Virginia 23681

Abstract

We present a zonal hybrid Reynolds-averaged Navier-Stokes (RANS) – large-eddy simulation (LES) strategy intended for application to problems involving turbulent flow separation. The methodology couples the standard k-ε linear eddy-viscosity RANS turbulence model with a two-equation nonlinear subgrid-scale (SGS) model for LES. The nonlinear SGS model requires the solutions of two transport equations for the subgrid turbulent kinetic energy and the subgrid viscous dissipation, which have the same structural form as the transport equations of the standard RANS k-ε model. Hence, the two transport equations for the total/subgrid turbulent kinetic energy and the total/subgrid viscous dissipation are solved in the entire domain with the coefficients of the production and destruction terms in the total/subgrid viscous dissipation transport equation set differently between the two zones. A source term is additionally included in the total viscous dissipation transport equation solved in the RANS zone and serves as a correction mechanism when the logarithmic-layer compatibility condition is not strictly satisfied among the RANS model coefficients. The coupling between the RANS and LES zones is accomplished by means of a smooth blending function that linearly combines the RANS and SGS turbulent stresses. A similar blending is also applied to the production, destruction and turbulent diffusion terms of the two transport equations. The blending function depends only on the wall-normal distance and the local maximum grid spacing. The proposed hybrid method applies the RANS calculation in the near-wall region and switches to the LES in the outer region; hence, it can be considered an alternative form of a wall-modeled LES. The present approach is free of the logarithmic-layer mismatch encountered in some other hybrid approaches, as well as the modeled-stress depletion that may occur in detached eddy simulation (DES) under certain circumstances. Application of the hybrid methodology to two benchmark test cases, which involve smooth-body flow separation around a Gaussian bump and a backward-facing smooth ramp, is demonstrated. It is shown that for the two test cases, the proposed methodology provides reasonable predictions at about three orders of magnitude lower computational cost relative to that of direct numerical simulation.

1 Introduction

Prediction of the turbulent flow separation induced by a severe adverse pressure gradient (APG) over a smoothly-contoured body is a challenging task due to the inherently complex and nonlinear nature of turbulence and the fundamental limitations of present turbulence models and computational tools. As this phenomenon is commonly encountered in many practical applications, its accurate prediction at an affordable computational cost has motivated research over several decades. While high-fidelity simulation techniques such as direct numerical simulation (DNS) and wall-resolved large-eddy simulation (WRLES) have shown good success in the prediction of canonical smooth-body flow separation problems, such tools will most likely remain prohibitively expensive for practical problems in the foreseeable future even though the era of exascale computing is already underway at the time of this writing. Meanwhile, lowest-fidelity turbulence simulations in the form of Reynolds-averaged Navier-Stokes (RANS) calculations, with many orders of magnitude lower computational cost relative to DNS or WRLES, have shown generally unsatisfactory performance in the prediction of separated flows. There is not yet a universal turbulence model; a model that works reasonably well in a particular scenario may perform poorly in another and thus require continuous recalibration from one problem to another. Given these issues, the intermediate-fidelity wall-modeled large-eddy simulation (WMLES) technique as well as various hybridized combinations of a RANS calculation with an LES, broadly classified as hybrid RANS-LES (HRLES), currently appear to be the most viable tools that can strike a reasonable balance between computational cost and solution accuracy in the prediction of turbulent separated flows.

A detailed review of numerous tried-and-tested variants of WMLES and HRLES with varying levels of complexity is beyond the scope of this work. Hence, we shall provide only a brief overview of some of these approaches. The simplest version of WMLES is based on either an algebraic wall model derived from the law-of-the-wall or an equilibrium wall model that solves a one-dimensional ordinary differential equation (ODE) along the wall-normal direction in the near-wall region [43, 26, 6]. More sophisticated non-equilibrium wall models of varying degrees of complexity proposed by several researchers are also available [39, 24, 3]. The wall model uses the instantaneous velocity at some distance from the wall to determine the wall viscous shear stress, which is then provided back to the outer region LES as a wall boundary condition. There is no correction applied to the turbulent stresses very near the wall, which is a region that is very poorly resolved by the WMLES grid. A review of the literature indicates that the simplest version of WMLES (based on the algebraic or the equilibrium wall model) is also the most commonly used since the incorporation of an algebraic or an ODE-based wall model into an existing flow solver is rather straightforward.

The degree of complexity of the HRLES technique, on the other hand, can vary depending on whether the method is zonal or non-zonal, the handling of the transition between the RANS calculation and the LES and the particular details of the RANS and LES models to be employed. The zonal approach applies the RANS calculation and the LES in separate regions. Unless some artificial forcing or synthetic turbulence is introduced at the interface between the two zones, the transition region usually contains a discontinuity in the numerical solution, which can manifest itself in the form of a logarithmic-layer mismatch [37]. Artificial forcing or synthetic turbulence introduced over the transition region enables a quicker switch between RANS and LES and helps alleviate the solution discontinuity over that region. A popular zonal HRLES technique commonly known as the detached eddy simulation (DES) and its variants [54, 55, 53] employ shielding functions to constrain the RANS calculation to at least some portion of the attached flow region or to its entirety while applying the LES elsewhere. The length scale of the RANS turbulence model is adjusted dynamically as the simulation switches from the RANS calculation to the LES so that the RANS turbulence model serves as the subgrid-scale (SGS) model in the LES region. An enhanced version of the original DES approach called the delayed detached eddy simulation (DDES) [55] attempts to eliminate the modeled-stress depletion [33, 54, 69] that arises when the switch from the RANS calculation to the LES occurs prematurely under certain circumstances and can lead to grid-induced flow separation. Other hybrid methods called the partially-averaged Navier-Stokes (PANS) calculation [20], the partially-integrated transport model (PITM) [48, 7] and the continuous RANS/LES approach [41, 42] are non-zonal methods that attempt to perform a more seamless coupling between the RANS calculation and the LES by making the transition dependent on a local "resolution indicator" quantity, such as the ratio between the modeled and the total turbulent kinetic energy. The RANS turbulence model of choice is modified to incorporate the resolution indicator in its formulation and serves as the global turbulence model that becomes the SGS model in the LES region. The main drawback of this type of approach is that the resolution indicator needed in the hybrid model formulation may be quite cumbersome to determine in complex flows.

It should be noted that with low-order methods, the algorithmic dissipation is often larger than that of the SGS model. The SGS model becomes more important when high-order methods with better dissipation characteristics are used. Hence, as will be discussed, a nonlinear SGS model, which we believe is likely to have the most benefit for high-order methods, is employed in combination with a fourth-order accurate spatial discretization scheme in the present study that pursues a zonal HRLES strategy with greater simplicity compared to other available variants. The proposed approach does not require the use of a resolution indicator. This alternate hybrid strategy is also chosen over WMLES based on equilibrium or non-equilibrium wall models for the following reasons: (a) As will be discussed, the SGS model used in this study requires the solution of a transport equation for the subgrid turbulent kinetic energy and another transport equation for the subgrid viscous dissipation. These two transport equations are structurally identical to those of the standard RANS k-ε turbulence model and therefore can be readily used for the application of the k-ε turbulence model in the near-wall region. Thus, a straightforward transformation of our LES solver implemented with the two transport equations to an HRLES solver based on the k-ε model was possible with minimal effort. In the current implementation, the RANS calculation is active in the near-wall region while the LES is active elsewhere. A blending function linearly combines the RANS and SGS turbulent stresses that appear in the governing equations. As will be discussed, a linear eddy-viscosity model is used in the RANS region and a nonlinear SGS model is used in the LES region; (b) Our nonlinear SGS model allows backscatter of energy from the modeled to the resolved scales. This backscatter helps break down the large-scale structures in the transition region between the RANS and LES zones, thus facilitating a relatively quick transition. This already built-in feature of the SGS model therefore simplifies the HRLES implementation and other measures such as artificial forcing or synthetic turbulence generation between the two zones are not needed; (c) In principle, an HRLES approach can potentially offer more accuracy than a typical WMLES that only makes use of the wall viscous shear stress provided by the wall model but does not make any corrections to the near-wall turbulent stresses. In contrast, the k-ε linear eddy-viscosity model applied near the wall in the present HRLES implementation provides both the wall viscous shear stress and the near-wall turbulent shear stress. Therefore, better accounting of the near-wall effect on the outer flow can be accomplished in this manner.

This paper describes the proposed HRLES methodology and demonstrates its application to two benchmark test cases that involve smooth-body flow separation around a Gaussian bump and a backward-facing smooth ramp. It is shown that for the two test cases, the proposed methodology provides reasonable predictions at about three orders of magnitude lower computational cost relative to that of DNS. The results also show that the present method does not suffer from logarithmic-layer mismatch and modeled-stress depletion issues. Areas of future improvement are identified and discussed. The paper is organized as follows. The details of the LES nonlinear SGS model and the RANS linear eddy-viscosity model are provided in Sections 2 and 3, respectively. The coupling between the RANS and LES zones is discussed in Section 4, and the boundary conditions needed for the solution of the two transport equations are described in Section 5. The pertinent details of the computational methodology are given in Section 6. The results obtained for the two test cases are analyzed in Sections 7 and 8. Section 9 summarizes the findings and provides the concluding remarks.

2 LES Nonlinear SGS Model

The LES SGS model used in this study is based on the dynamic nonlinear model that was previously proposed by Uzun and Malik [64]. The original version of this model requires test filtering of the resolved flowfield using two different test-filter widths for the dynamic computation of the model coefficients. Since test filtering of the resolved flowfield using two different filter widths can be impractical or difficult under certain circumstances, the present study employs a slightly revised version of the model that requires test filtering of the resolved flowfield using a single test-filter width. As also discussed in Uzun and Malik [64], the present nonlinear model, inspired by the original triple model idea of Bardina et al. [5], includes a Galilean-invariant term called the modified Leonard stress tensor and two nonlinear terms based on the products of the strain-rate and rotation-rate tensors for an improved representation of the subgrid-scale dissipation, backscatter and anisotropy effects. Furthermore, as will be discussed, the model does not employ any *ad hoc* averaging or clipping procedures and does not require the specification of a characteristic length scale; hence, it avoids the ambiguities associated with defining a proper length scale for anisotropic grids.

For compressible flows, the flowfield variables are expressed in terms of Favre-filtered quantities [14]. A Favre-filtered quantity is defined as $\tilde{f} = \overline{\rho f}/\overline{\rho}$, where ρ is the fluid density, f is the unfiltered variable, $\tilde{f}$ is the Favre-filtered variable and the overline denotes a spatial filtering operation. The governing equations to be solved for the evolution of the compressible flow are formulated in terms of the Favre-filtered flow variables. The corresponding SGS stress tensor that appears in the governing equations is given by

$$\tau_{ij} = \overline{\rho u_i u_j} - \frac{\overline{\rho u_i}\,\overline{\rho u_j}}{\overline{\rho}} = \overline{\rho}\left(\widetilde{u_i u_j} - \tilde{u}_i \tilde{u}_j\right) \tag{1}$$

where $\overline{(\ )}$ now denotes the implicit grid filter imposed by the application of the numerical discretization scheme on a local grid resolution of Δ, $\widetilde{(\ )}$ is the corresponding Favre filter and u_i is the unfiltered velocity component.

The nonlinear SGS model has the following form

$$\tau_{ij}^{LES} - \frac{2}{3}\overline{\rho} k_{sgs} \delta_{ij} = C_1 \frac{\overline{\rho} k_{sgs}}{\mathcal{L}_{kk}^m}\left(\mathcal{L}_{ij}^m - \frac{\delta_{ij}}{3}\mathcal{L}_{kk}^m\right) + C_2 \frac{\overline{\rho} k_{sgs}}{|\widetilde{M}|}\widetilde{M}_{ij} + C_3 \frac{\overline{\rho} k_{sgs}}{|\widetilde{N}|}\widetilde{N}_{ij} \tag{2}$$

where

$$\mathcal{L}_{ij}^m = \overline{\overline{\rho}\tilde{u}_i\tilde{u}_j} - \frac{\overline{\overline{\rho}\tilde{u}_i}\,\overline{\overline{\rho}\tilde{u}_j}}{\overline{\overline{\rho}}} \tag{3}$$

is the compressible version of the modified Leonard stress tensor, which is Galilean invariant [18, 30], as are the other terms of the model, and $\overline{\rho}$ is the grid-filtered or resolved density. The uppermost $\overline{(\ )}$ in the $\mathcal{L}_{ij}^m$ expression indicates explicit spatial filtering at a scale that is equal to the grid-filter width, which is taken the same as the local grid spacing, Δ. The model coefficients C_1, C_2, C_3 are determined using a localized dynamic procedure, which requires test filtering of the resolved flowfield, as will be discussed. The SGS turbulent kinetic energy, $k_{sgs} = 0.5\tau_{kk}^{LES}/\overline{\rho}$, appearing in Eq. (2) is obtained from the solution of a transport equation to be introduced along with another transport equation for the subgrid viscous dissipation, ε_{sgs}. The tensors $\widetilde{M}_{ij}$ and $\widetilde{N}_{ij}$ in Eq. (2) are defined as

$$\widetilde{M}_{ij} = \widetilde{S}_{ik}\widetilde{S}_{kj} - \frac{\delta_{ij}}{3}\widetilde{S}_{kl}\widetilde{S}_{kl}\ , \quad \widetilde{N}_{ij} = \widetilde{S}_{ik}\widetilde{\Omega}_{kj} - \widetilde{\Omega}_{ik}\widetilde{S}_{kj} \tag{4}$$

with $|\widetilde{M}| = \left(\widetilde{M}_{ij}\widetilde{M}_{ij}\right)^{1/2}$, $|\widetilde{N}| = \left(\widetilde{N}_{ij}\widetilde{N}_{ij}\right)^{1/2}$. $\widetilde{S}_{ij}$ and $\widetilde{\Omega}_{ij}$ are the resolved strain-rate and rotation-rate tensors, respectively, given by

$$\widetilde{S}_{ij} = \frac{1}{2}\left(\frac{\partial \tilde{u}_i}{\partial x_j} + \frac{\partial \tilde{u}_j}{\partial x_i}\right)\ , \quad \widetilde{\Omega}_{ij} = \frac{1}{2}\left(\frac{\partial \tilde{u}_i}{\partial x_j} - \frac{\partial \tilde{u}_j}{\partial x_i}\right)\ . \tag{5}$$

Note that in the above tensor expressions, the tilde symbol over a tensor is meant to indicate that the tensor is based on the spatial derivatives of the Favre-filtered velocity components.

There is no characteristic length scale appearing in the second and third terms on the right-hand side of Eq. (2). Instead, those terms contain $\overline{\rho} k_{sgs}$ and are normalized by either $|\widetilde{M}|$ or $|\widetilde{N}|$ for dimensional consistency*. We do not use a length scale in our formulation because the matter of defining the most

*Note that either or both denominators may become zero in case a uniform inviscid or an irrotational region were to exist in the immediate vicinity of the turbulent flow under investigation but such a scenario is unlikely in the problems for which the present model is intended. A very small number may be added to the denominator to avoid division by zero if necessary. Another option is to set the model coefficients to zero if a singularity were to occur since such a scenario would only arise outside a turbulent region.

appropriate length scale for anisotropic grids is far from being resolved. For example, in the study by Schumann et al. [50], several different length scales, including the most commonly-used cubic-root of the cell volume as well as the local maximum grid spacing among other choices, were considered in the LES of turbulent channel flows. It was found that while some length scales performed better than others, none produced results independent of the grid anisotropy. Such unresolved issues are avoided altogether in the present model as its formulation does not require the specification of a length scale.

To derive an equation that can be used to compute the model coefficients, we first assume that the constitutive relationship given in Eq. (2) for subgrid scales is also valid at larger scales, which are several times the size of the largest subgrid scales. We can therefore write the following relationship, which has the same structure as Eq. (2) with the same coefficients

$$T_{ij} - \frac{\delta_{ij}}{3} T_{kk} = C_1 \frac{0.5 T_{kk}}{H_{kk}} \left(H_{ij} - \frac{\delta_{ij}}{3} H_{kk} \right) + C_2 \frac{0.5 T_{kk}}{|\widehat{M}|} \widehat{M}_{ij} + C_3 \frac{0.5 T_{kk}}{|\widehat{N}|} \widehat{N}_{ij} \tag{6}$$

where

$$T_{ij} = \widehat{\rho u_i u_j} - \frac{\widehat{\rho u_i}\, \widehat{\rho u_j}}{\widehat{\rho}} , \quad H_{ij} = \widehat{\widehat{\rho} \hat{u}_i \hat{u}_j} - \frac{\widehat{\widehat{\rho} \hat{u}_i}\, \widehat{\widehat{\rho} \hat{u}_j}}{\widehat{\widehat{\rho}}} , \quad \hat{u}_i = \frac{\widehat{\rho u_i}}{\widehat{\rho}} , \tag{7}$$

$$\widehat{M}_{ij} = \widehat{S}_{ik} \widehat{S}_{kj} - \frac{\delta_{ij}}{3} \widehat{S}_{kl} \widehat{S}_{kl} , \quad \widehat{N}_{ij} = \widehat{S}_{ik} \widehat{\Omega}_{kj} - \widehat{\Omega}_{ik} \widehat{S}_{kj} , \quad |\widehat{M}| = \left(\widehat{M}_{ij} \widehat{M}_{ij} \right)^{1/2} , \quad |\widehat{N}| = \left(\widehat{N}_{ij} \widehat{N}_{ij} \right)^{1/2} , \tag{8}$$

$$\widehat{S}_{ij} = \frac{1}{2} \left(\frac{\partial \hat{u}_i}{\partial x_j} + \frac{\partial \hat{u}_j}{\partial x_i} \right) , \quad \widehat{\Omega}_{ij} = \frac{1}{2} \left(\frac{\partial \hat{u}_i}{\partial x_j} - \frac{\partial \hat{u}_j}{\partial x_i} \right) . \tag{9}$$

In the above formulation, the filtering operation denoted by $\widehat{(\ )}$ has a width that is larger than the local grid-filter width. Analogous to Eq. (2), the quantities to be filtered for the evaluation of H_{ij} are constructed from the flowfield variables extracted at the filter level of the left-hand side term, which is $\widehat{(\ )}$. Likewise, the tensors appearing in the second and third terms on the right-hand side are evaluated using the velocity field extracted at the $\widehat{(\ )}$ level.

Equation (6) cannot be applied directly in an LES because the unfiltered flowfield denoted by u_i and ρ would be unavailable for the filtering operations needed to evaluate the terms in that equation. In order to make use of the above constitutive relationship to compute the model coefficients, we further assume that this relationship holds true after u_i is replaced with $\tilde{u}_i$ and ρ with $\overline{\rho}$. After these substitutions, we have

$$L^m_{ij} - \frac{\delta_{ij}}{3} L^m_{kk} = C_1 \frac{0.5 L^m_{kk}}{\mathscr{L}^m_{kk}} \left(\mathscr{L}^m_{ij} - \frac{\delta_{ij}}{3} \mathscr{L}^m_{kk} \right) + C_2 \frac{0.5 L^m_{kk}}{|\widehat{\widetilde{M}}|} \widehat{\widetilde{M}}_{ij} + C_3 \frac{0.5 L^m_{kk}}{|\widehat{\widetilde{N}}|} \widehat{\widetilde{N}}_{ij} \tag{10}$$

where

$$L^m_{ij} = \widehat{\overline{\rho} \tilde{u}_i \tilde{u}_j} - \frac{\widehat{\overline{\rho} \tilde{u}_i}\, \widehat{\overline{\rho} \tilde{u}_j}}{\widehat{\overline{\rho}}} , \quad \mathscr{L}^m_{ij} = \widehat{\widehat{\overline{\rho}} \hat{\tilde{u}}_i \hat{\tilde{u}}_j} - \frac{\widehat{\widehat{\overline{\rho}} \hat{\tilde{u}}_i}\, \widehat{\widehat{\overline{\rho}} \hat{\tilde{u}}_j}}{\widehat{\widehat{\overline{\rho}}}} , \quad \hat{\tilde{u}}_i = \frac{\widehat{\overline{\rho} \tilde{u}_i}}{\widehat{\overline{\rho}}} , \tag{11}$$

$$\widehat{\widetilde{M}}_{ij} = \widehat{\widetilde{S}}_{ik} \widehat{\widetilde{S}}_{kj} - \frac{\delta_{ij}}{3} \widehat{\widetilde{S}}_{kl} \widehat{\widetilde{S}}_{kl} , \quad \widehat{\widetilde{N}}_{ij} = \widehat{\widetilde{S}}_{ik} \widehat{\widetilde{\Omega}}_{kj} - \widehat{\widetilde{\Omega}}_{ik} \widehat{\widetilde{S}}_{kj} , \quad |\widehat{\widetilde{M}}| = \left(\widehat{\widetilde{M}}_{ij} \widehat{\widetilde{M}}_{ij} \right)^{1/2} , \quad |\widehat{\widetilde{N}}| = \left(\widehat{\widetilde{N}}_{ij} \widehat{\widetilde{N}}_{ij} \right)^{1/2} , \tag{12}$$

$$\widehat{\widetilde{S}}_{ij} = \frac{1}{2} \left(\frac{\partial \hat{\tilde{u}}_i}{\partial x_j} + \frac{\partial \hat{\tilde{u}}_j}{\partial x_i} \right) , \quad \widehat{\widetilde{\Omega}}_{ij} = \frac{1}{2} \left(\frac{\partial \hat{\tilde{u}}_i}{\partial x_j} - \frac{\partial \hat{\tilde{u}}_j}{\partial x_i} \right) . \tag{13}$$

Note that the "Germano identity" [19] has not been invoked anywhere during the derivation of the above equations; thus, we avoid a formulation in which the model coefficients appear inside a filtering operation. The usual practice in models derived using the Germano identity has been to pull the model coefficient out of the test-filtering operation as if it were a constant, which is of course in direct contradiction with the spatially-varying nature of the model coefficient. Some *ad hoc* averaging or clipping procedures are then needed to maintain numerical stability in those models. The present model does not suffer from such an inconsistency. The ratio of the test-filter width to the grid-filter width is a free parameter. Its value is typically chosen as 2 for most LES; we also set the test-filter width to 2Δ here. Using the test-filtered quantities, we can evaluate all of the terms appearing in Eq. (10), which are then used to solve for C_1, C_2, C_3.

Due to the L^m_{ij} tensor symmetry, Eq. (10) gives rise to a linear system of six equations with three unknowns. As there are fewer unknowns than knowns, a least-squares approach [29] can be used to minimize the error in the computed model coefficients. Let E_{ij} be the associated error of the overdetermined system, given by

$$E_{ij} = L^d_{ij} - C_1 \mathscr{L}^d_{ij} - C_2 \gamma_{ij} - C_3 \lambda_{ij} \tag{14}$$

where

$$L^d_{ij} = L^m_{ij} - \frac{\delta_{ij}}{3} L^m_{kk} , \quad \mathscr{L}^d_{ij} = \frac{0.5 L^m_{kk}}{\mathscr{L}^m_{kk}} \left(\mathscr{L}^m_{ij} - \frac{\delta_{ij}}{3} \mathscr{L}^m_{kk} \right) , \quad \gamma_{ij} = \frac{0.5 L^m_{kk}}{|\widehat{\widetilde{M}}|} \widehat{\widetilde{M}}_{ij} , \quad \lambda_{ij} = \frac{0.5 L^m_{kk}}{|\widehat{\widetilde{N}}|} \widehat{\widetilde{N}}_{ij} . \tag{15}$$

The squared error is $Q = E_{ij} E_{ij} = \left(L^d_{ij} - C_1 \mathscr{L}^d_{ij} - C_2 \gamma_{ij} - C_3 \lambda_{ij} \right)^2$. The optimum coefficients are determined by the constraint that minimizes the squared error [29], with

$$\frac{\partial Q}{\partial C_i} = 0 \quad (i = 1, 2, 3) . \tag{16}$$

Application of the above criterion then leads to the following 3×3 linear system, the solution of which provides the dynamic model coefficients in a localized manner.

$$\begin{bmatrix} \mathscr{L}^d_{ij} \mathscr{L}^d_{ij} & \mathscr{L}^d_{ij} \gamma_{ij} & \mathscr{L}^d_{ij} \lambda_{ij} \\ \gamma_{ij} \mathscr{L}^d_{ij} & \gamma_{ij} \gamma_{ij} & \gamma_{ij} \lambda_{ij} \\ \lambda_{ij} \mathscr{L}^d_{ij} & \lambda_{ij} \gamma_{ij} & \lambda_{ij} \lambda_{ij} \end{bmatrix} \begin{bmatrix} C_1 \\ C_2 \\ C_3 \end{bmatrix} = \begin{bmatrix} L^d_{ij} \mathscr{L}^d_{ij} \\ L^d_{ij} \gamma_{ij} \\ L^d_{ij} \lambda_{ij} \end{bmatrix} . \tag{17}$$

2.1 Test Filtering for the Dynamic Evaluation of SGS Model Coefficients

Dynamic evaluation of the SGS model coefficients requires test filtering of the resolved flowfield using a test-filter width that is taken as twice the grid-filter width. The local grid-filter width is assumed the same as the local grid spacing. For LES based on finite-difference schemes, Shah [52] derived a 3-point box filter, applicable on structured grids, that takes the nonuniform grid spacings into account. The coefficients of the filter were determined analytically by Shah [52] using Taylor series expansions and matching of the coefficients that appear on the two sides of the equation derived for the filtered quantity. We follow the universal procedure of Shah [52] to derive a 7-point explicit central box filter applicable to any structured grid. The filter coefficients, which depend on the specified ratio between the filter width and the local grid spacing, are determined numerically rather than analytically. This 7-point central filter accounts for nonuniform grid spacings and allows test filtering with a maximum width of 6Δ on a uniform grid. On nonuniform grids, assuming the grid spacing variation along a given direction is gradual, the maximum filter width is also about 6Δ. Proper one-sided and biased explicit formulations are derived for the grid points located near physical boundaries. In three dimensions, the filter is applied successively along the curvilinear grid lines of a structured grid. The corresponding test-filter coefficients are determined separately for each direction based on the local grid spacings and the chosen filter width. Filtering on physical boundaries is performed only along the two transverse directions. It should be remarked that these procedures developed for structured grids are not directly applicable to unstructured grids.

2.2 Transport Equations for the SGS Turbulent Kinetic Energy and SGS Viscous Dissipation

The SGS turbulent kinetic energy, k_{sgs}, needed in the model formulation is obtained from the solution of a transport equation for k_{sgs} [9, 51], which is given by

$$\frac{\partial \overline{\rho} k_{sgs}}{\partial t} + \frac{\partial \overline{\rho} \tilde{u}_i k_{sgs}}{\partial x_i} = P^+_{k_{sgs}} + P^-_{k_{sgs}} + \frac{\partial}{\partial x_i}\left[\left(\tilde{\mu} + \frac{\mu_t}{\sigma_{k_{sgs}}}\right)\frac{\partial k_{sgs}}{\partial x_i}\right] - \overline{\rho}\varepsilon_{sgs} \tag{18}$$

where the four terms on the right-hand side represent the positive production (forward scatter), negative production (backward scatter), diffusion (or spatial redistribution) and viscous dissipation of k_{sgs}, respectively. $\tilde{\mu}$ is the molecular viscosity, μ_t is the eddy viscosity and $\sigma_{k_{sgs}}$ is the turbulent diffusion coefficient for k_{sgs}. As our model allows both forward and backward scatter of energy between the resolved and modeled scales, the net production of k_{sgs} is given by the sum of the positive and negative production terms as

$$P_{k_{sgs}} = P^+_{k_{sgs}} + P^-_{k_{sgs}} = -\tau^{LES}_{ij}\widetilde{S}_{ij} \tag{19}$$

where

$$P^+_{k_{sgs}} = -\tau^{LES}_{ij}\widetilde{S}_{ij} \quad \text{if} \;\; -\tau^{LES}_{ij}\widetilde{S}_{ij} > 0\ , \qquad P^-_{k_{sgs}} = -\tau^{LES}_{ij}\widetilde{S}_{ij} \quad \text{if} \;\; -\tau^{LES}_{ij}\widetilde{S}_{ij} < 0 \tag{20}$$

and τ^{LES}_{ij} is taken from Eq. (2). The diffusion term includes the viscous diffusion and the combined model for turbulent transport and pressure diffusion, which is based on the gradient-diffusion hypothesis. The eddy viscosity which appears in the modeled diffusion term is determined using the following relation [2]

$$-\left(\tau^{LES}_{ij} - \frac{2}{3}\overline{\rho} k_{sgs}\delta_{ij}\right)\widetilde{S}_{ij} = 2\mu_t \widetilde{S}^d_{ij}\widetilde{S}_{ij}\ . \tag{21}$$

This relation gives the equivalent eddy viscosity, μ_t, of a linear eddy-viscosity model that produces the same net energy scatter as that by the deviatoric component of our nonlinear model. However, it does not guarantee a positive μ_t value at all times. As the concept of a negative eddy viscosity lacks rigorous justification, the equivalent eddy viscosity determined above is not allowed to become negative; hence, clipping to zero is enforced whenever the above identity produces a negative μ_t value.

Closure of the above transport equation for k_{sgs} requires a model for the SGS viscous dissipation, ε_{sgs}. Although some fairly simple algebraic models are available for ε_{sgs}, the performance of such models was found unsatisfactory in the problems investigated during the course of this study as they did not lead to an accurate free shear layer growth rate in the separated flow regions resolved by LES. Therefore, a separate transport equation for ε_{sgs} is solved, which is given by

$$\frac{\partial \overline{\rho}\varepsilon_{sgs}}{\partial t} + \frac{\partial \overline{\rho}\tilde{u}_i\varepsilon_{sgs}}{\partial x_i} = \frac{C_{\varepsilon_1}}{T_t}P^+_{k_{sgs}} + \frac{\partial}{\partial x_i}\left[\left(\tilde{\mu} + \frac{\mu_t}{\sigma_{\varepsilon_{sgs}}}\right)\frac{\partial \varepsilon_{sgs}}{\partial x_i}\right] - \frac{C_{\varepsilon_2}}{T_t}\left(\overline{\rho}\varepsilon_{sgs} - P^-_{k_{sgs}}\right) \tag{22}$$

where the three terms on the right-hand side represent the production, diffusion and destruction of ε_{sgs}, respectively. $\sigma_{\varepsilon_{sgs}}$ is the turbulent diffusion coefficient for ε_{sgs} and C_{ε_1} and C_{ε_2} are the coefficients of the production and destruction terms, respectively. The diffusion term contains the viscous diffusion of ε_{sgs} and the combined model for turbulent transport and pressure diffusion based on the gradient-diffusion hypothesis. T_t is the hybrid time scale [70] defined as

$$T_t = \frac{k_{sgs}}{\varepsilon_{sgs}} + \sqrt{\frac{\tilde{\mu}}{\overline{\rho}\varepsilon_{sgs}}}\ . \tag{23}$$

The first term on the right-hand side of the above expression is the turbulent time scale and the second term is the viscous or the Kolmogorov time scale. To avoid a singularity in the dissipation transport equation as k_{sgs} approaches zero, T_t is taken as the sum of the turbulent and viscous time scales.

The transport equation for ε_{sgs} is very similar in structure to the analogous dissipation transport equation of the RANS k-ε turbulence model [22, 23, 27], except for one important distinction. As our nonlinear SGS model allows both forward and backward scatter of energy between the resolved and subgrid scales, the effect of these two processes on the production and destruction of dissipation is taken separately into account. Hence, the production term of Eq. (22) depends only on the positive production of k_{sgs} or $P^+_{k_{sgs}}$. This is in accordance with the assumption that the production of viscous dissipation is proportional to the positive production of turbulent kinetic energy or the forward scattered energy. On the other hand, the destruction term in Eq. 22 is set to depend on both ε_{sgs} and the negative production of k_{sgs} or $P^-_{k_{sgs}}$ because both ε_{sgs} and $P^-_{k_{sgs}}$ will cause a reduction in the local k_{sgs}, which will subsequently have a decreasing effect on the local ε_{sgs}.

The error in the dynamic model coefficients, which originates from solving an overdetermined system using the least-squares approach, creates the possibility of excessive forward or backward scatter of energy between the resolved and subgrid scales at isolated instants during the simulation. This may, in turn, lead to numerical instability. To deal with this matter, a production limiter derived from the realizability constraints of the modeled stresses can be imposed. Mokhtarpoor and Heinz [36] showed that for a linear eddy-viscosity model, in order for the modeled stresses to satisfy the realizability constraints, the eddy-viscosity magnitude should be bounded as

$$| \mu_t | \leq \frac{23}{24\sqrt{3}} \frac{\overline{\rho} k_{sgs}}{|\widetilde{S}|^d} \tag{24}$$

where

$$|\widetilde{S}|^d = \left(2\widetilde{S}^d_{ij}\widetilde{S}^d_{ij}\right)^{1/2} , \quad \widetilde{S}^d_{ij} = \widetilde{S}_{ij} - \frac{\delta_{ij}}{3}\widetilde{S}_{kk} . \tag{25}$$

On the other hand, Vreman et al. [68] as well as Kim and Menon [25] among others derived the following value based on an alternate analysis of the realizability constraints

$$| \mu_t | \leq \frac{2}{\sqrt{3}} \frac{\overline{\rho} k_{sgs}}{|\widetilde{S}|^d} . \tag{26}$$

Note that this limit is about double the value found by Mokhtarpoor and Heinz [36]. In any case, given a certain eddy-viscosity limit, μ_t^{max}, we can determine the maximum allowable positive production of k_{sgs} (i.e., forward scatter) as

$$P^{+^{limit}}_{k_{sgs}} = -\left(-2\mu_t^{max}\widetilde{S}^d_{ij} + \frac{2}{3}\overline{\rho} k_{sgs}\delta_{ij}\right)\widetilde{S}_{ij} = 2\mu_t^{max}(\widetilde{S}^d_{ij}\,\widetilde{S}_{ij}) - \frac{2}{3}\overline{\rho} k_{sgs}\widetilde{S}_{kk} . \tag{27}$$

Similarly, the limiter magnitude for the negative production of k_{sgs} (i.e., backward scatter) is determined as

$$P^{-^{limit}}_{k_{sgs}} = -2\mu_t^{max}(\widetilde{S}^d_{ij}\,\widetilde{S}_{ij}) - \frac{2}{3}\overline{\rho} k_{sgs}\widetilde{S}_{kk} . \tag{28}$$

As stated in the discussion of Eq. (21), the positive or negative production of k_{sgs} by the deviatoric component of our nonlinear model can be represented by a linear model with an equivalent eddy viscosity. Thus, the above production limiters derived for a linear model are assumed to be applicable to the present nonlinear model. As the higher value of μ_t^{max} would be less intrusive than the lower value, in this study we opt to take

$$\mu_t^{max} = \frac{2}{\sqrt{3}} \frac{\overline{\rho} k_{sgs}}{|\widetilde{S}|^d} . \tag{29}$$

Whenever a positive or negative production limiter is enforced, all relevant SGS stress components that contribute to the positive or negative production are properly rescaled so that the associated tensor product sum, $-\tau_{ij}^{LES}\widetilde{S}_{ij}$, becomes equal to the imposed limit. Other than this production term limiter procedure, no spatial/temporal averaging or clipping of the dynamic nonlinear model coefficients is employed. The limiter-constrained values of $P^{+}_{k_{sgs}}$ and $P^{-}_{k_{sgs}}$ are used in both transport equations.

We now discuss the setting of the coefficients that appear in the transport equations solved in the LES region. Since viscous dissipation occurs at length scales that are much smaller than those resolved in a typical coarse-grid LES, setting of the C_{ε_1} and C_{ε_2} coefficients in the ε_{sgs} transport equation is highly empirical in nature. Although Gallerano et al. [17] proposed a dynamic procedure to evaluate C_{ε_1} and C_{ε_2} within the framework of a two-equation LES SGS model, this dynamic evaluation of the two coefficients works only when the LES grid resolves at least part of the dissipative length scale range so that the scale-similarity assumption can be invoked. On very coarse grids or at infinite Reynolds number, wherein none of the dissipative length scales are resolved, such dynamic determination of C_{ε_1} and C_{ε_2} via test filtering is not possible since the resolved flowfield cannot provide any information pertaining to the dissipative length scale range. As the current hybrid model is intended for applications involving rather coarse grids in general, various strategies for the setting of C_{ε_1} and C_{ε_2} based on empirical correlations were investigated in this study. In the current implementation, following the proposal of Durbin [10, 11], the coefficient of the production term, C_{ε_1}, is set as follows

$$C_{\varepsilon_1} = C^{*}_{\varepsilon_1}\left(1 + 0.1\frac{P^{+}_{k_{sgs}}}{\varepsilon_{sgs}}\right) \quad \text{where} \quad C^{*}_{\varepsilon_1} = \frac{1.44}{1.1} \,. \tag{30}$$

The above formulation makes C_{ε_1} dependent upon the ratio between the positive production of k_{sgs} and ε_{sgs}; when $P^{+}_{k_{sgs}} = \varepsilon_{sgs}$, C_{ε_1} becomes 1.44, which is the same as the standard value used in the RANS calculation of free shear layers with the k-ε model [27]. The coefficient of the destruction term, C_{ε_2}, is set following the work of Perot and Gadebusch [41, 42], who proposed a continuous two-equation RANS/LES model that is valid at any mesh resolution. To reiterate, their model is based on a resolution indicator that requires an estimate of the ratio between the modeled and the total turbulent kinetic energy. The destruction term coefficient is given by

$$C_{\varepsilon_2} = \frac{11}{6}f + \frac{25}{Re_T}f^2 \quad \text{where} \;\; f = \frac{Re_T}{30}\left[\sqrt{1 + \frac{60}{Re_T}} - 1\right] \tag{31}$$

and Re_T is the unresolved turbulence Reynolds number defined as $Re_T = \bar{\rho}k^2_{sgs}/\left(\tilde{\mu}\varepsilon_{sgs}\right)$. The above formulation varies C_{ε_2} as a function of Re_T. It gives the theoretical value of $C_{\varepsilon_2} = 11/6$ at high Re_T and $5/3$ as $Re_T \to 0$. The turbulent diffusion coefficients in the transport equations solved in the LES region are set to $\sigma_{k_{sgs}} = 1$ and $\sigma_{\varepsilon_{sgs}} = 1.2$, which are among the commonly used values [41, 42].

3 RANS Linear Eddy-Viscosity Turbulence Model

The details of the RANS turbulence model are provided next. As noted earlier, in the present zonal hybrid method implementation, the RANS calculation is active in the near-wall region, where the following linear eddy-viscosity model is employed to compute the RANS turbulent stresses

$$\tau_{ij}^{RANS} = \frac{2}{3}\rho K\delta_{ij} - 2\mu_t^{RANS}\left(S_{ij} - \frac{1}{3}S_{kk}\delta_{ij}\right) \quad \text{where} \;\; S_{ij} = \frac{1}{2}\left(\frac{\partial U_i}{\partial x_j} + \frac{\partial U_j}{\partial x_i}\right)\,, \tag{32}$$

U_i denotes the velocity components of the RANS solution, μ_t^{RANS} is the turbulent eddy viscosity, ρ is the density and K is the total turbulent kinetic energy.[†] The turbulent eddy viscosity is given by

$$\mu_t^{RANS} = \rho C_\mu f_\mu \frac{K^2}{\varepsilon} \quad \text{where} \quad C_\mu = 0.09 \tag{33}$$

[†]The uppercase K is used here to differentiate the total turbulent kinetic energy from k_{sgs}.

and f_μ is the following near-wall damping function proposed by Fan et al. [13]

$$f_\mu = 0.4\frac{f_w}{\sqrt{Re_T}} + \left(1 - 0.4\frac{f_w}{\sqrt{Re_T}}\right)\left[1 - \exp\left(-\frac{Re_d}{42.63}\right)\right]^3 \tag{34}$$

where $Re_d = \sqrt{K}d/\nu$ is a turbulent Reynolds number based on the velocity scale $\sqrt{K}$ and the wall-normal distance, d, Re_T is the unresolved turbulence Reynolds number defined as $Re_T = K^2/(\nu\varepsilon)$, $\nu = \mu/\rho$ is the kinematic viscosity and

$$f_w = 1 - \exp\left\{-\frac{\sqrt{Re_d}}{2.3} + \left(\frac{\sqrt{Re_d}}{2.3} - \frac{Re_d}{8.89}\right)\left[1 - \exp\left(-\frac{Re_d}{20}\right)\right]^3\right\} \, . \tag{35}$$

An eddy-viscosity limiter analogous to Eq. (26) is imposed on μ_t^{RANS} as follows

$$\mu_t^{RANS} \leq \frac{2}{\sqrt{3}}\frac{\rho K}{|S|^d} \quad \text{where} \quad |S|^d = \left(2S_{ij}^d S_{ij}^d\right)^{1/2} \, , \quad S_{ij}^d = S_{ij} - \frac{\delta_{ij}}{3}S_{kk} \, . \tag{36}$$

3.1 Transport Equations for the Total Turbulent Kinetic Energy and the Total Viscous Dissipation

The analogous transport equations for the total turbulent kinetic energy, K, and the total viscous dissipation, ε, applicable in the RANS region are given by

$$\frac{\partial \rho K}{\partial t} + \frac{\partial \rho U_i K}{\partial x_i} = P_K^{RANS} + \frac{\partial}{\partial x_i}\left[\left(\mu + \sigma_K^{-1}\mu_t^{RANS}\right)\frac{\partial K}{\partial x_i}\right] - \rho\varepsilon \tag{37}$$

$$\frac{\partial \rho \varepsilon}{\partial t} + \frac{\partial \rho U_i \varepsilon}{\partial x_i} = \frac{C_{\varepsilon_1}^{RANS}}{T_t}P_K^{RANS} + \frac{\partial}{\partial x_i}\left[\left(\mu + \sigma_\varepsilon^{-1}\mu_t^{RANS}\right)\frac{\partial \varepsilon}{\partial x_i}\right] - \frac{C_{\varepsilon_2}^{RANS}}{T_t}\rho\varepsilon f_\varepsilon + S_\varepsilon \tag{38}$$

where $P_K^{RANS} = -\tau_{ij}^{RANS}S_{ij}$ is the production of turbulent kinetic energy, T_t is the hybrid time scale [70] defined as $T_t = K/\varepsilon + \sqrt{\nu/\varepsilon}$ and f_ε is a damping function that is expressed as the product of two functions in the form of $f_\varepsilon = f_1 \cdot f_2$. The first function sensitizes $C_{\varepsilon_2}^{RANS}$ to low Re_T values in the vicinity the wall and is taken as $f_1 = 1 - 0.3\exp\left[-Re_T^2\right]$ [40] while the second function provides $\mathcal{O}(d^2)$ damping of ε near the wall [13] as the production of dissipation vanishes there. It is given by $f_2 = f_w^2$, where f_w is defined in Eq. (35). σ_K and σ_ε are the turbulent diffusion coefficients for K and ε, respectively.

The source term S_ε that appears in Eq. (38) is given by [44, 38]

$$S_\varepsilon = \frac{\rho u_\tau^4}{d^2}\left[\left(C_{\varepsilon_2}^{RANS} - C_{\varepsilon_1}^{RANS}\right)\frac{\sqrt{C_\mu}}{\kappa^2} - \sigma_\varepsilon^{-1}\right] \cdot f_d \tag{39}$$

where u_τ is the friction velocity at the nearest wall location, κ is the von Kármán constant and f_d is a damping function with a value between 0 and 1, the more specific details of which are to be discussed. This source term originates from the following expression, to which the dissipation transport equation reduces in the logarithmic layer of a turbulent boundary layer under a zero pressure gradient (ZPG), as shown by Richards and Hoxey [47]

$$\frac{\rho u_\tau^4}{d^2}\left[\left(C_{\varepsilon_1}^{RANS} - C_{\varepsilon_2}^{RANS}\right)\frac{\sqrt{C_\mu}}{\kappa^2} + \sigma_\varepsilon^{-1}\right] = 0 \, . \tag{40}$$

The above expression leads to the following compatibility condition [27, 47] among the chosen model coefficients

$$C_{\varepsilon_2}^{RANS} - C_{\varepsilon_1}^{RANS} = \sigma_\varepsilon^{-1}\frac{\kappa^2}{\sqrt{C_\mu}} \, . \tag{41}$$

When a given combination of the chosen model coefficients does not satisfy the compatibility condition, Eq. 40 no longer holds. Hence, in such a case, the addition of S_ε (with $f_d = 1$) to the left-hand side of Eq. 40 would provide a zero net sum. When the compatibility condition is satisfied, the source term magnitude becomes zero. As Eq. (40) is strictly valid in the logarithmic layer, the damping function used in Eq. (39), f_d, should be designed such that it takes a value of 1 in the logarithmic layer and decays to 0 away from the logarithmic layer. For f_d, we repurpose the blending function employed in Menter's improved k-ω turbulence models [31, 32], which is originally referred to as F_1 in Menter's work. Our damping function is defined as $f_d = \tanh\left[(\ell_t/d)^4\right]$, where ℓ_t is the turbulence length scale given by $\ell_t = K^{3/2}/\varepsilon$. Our f_d is identical to Menter's F_1 in the logarithmic layer; it takes a value of 1 in the logarithmic layer and quickly decays to 0 as the wall is approached. Note that Menter's more sophisticated F_1 switches to another quantity in the argument of the hyperbolic-tangent function to enforce $F_1 = 1$ in the viscous sublayer, which is not needed here. It should be also remarked that the friction velocity at the nearest wall location, u_τ, that is needed for the evaluation of S_ε may be cumbersome to determine under certain circumstances. In the present implementation, u_τ is therefore estimated by assuming a constant stress layer within the RANS region, in which the sum of the viscous shear stress and the turbulent shear stress at a given off the wall location is taken to be equivalent to the viscous shear stress at the nearest wall location. The friction velocity is then obtained from the computed total shear stress. Note that in the logarithmic layer, the viscous shear stress is negligible and the total shear stress can therefore be taken the same as the turbulent shear stress.

We now discuss the setting of the model coefficients in the RANS zone. The usual practice in most RANS calculations has been to set $C_{\varepsilon_1}^{RANS}$ and $C_{\varepsilon_2}^{RANS}$ to some static values, which are located within a range of values based on empirical observations. The standard high Reynolds number value of $C_{\varepsilon_1}^{RANS}$ is normally taken as 1.44 or 1.45 in free shear layers [27, 40]. For wall-bounded flows, $C_{\varepsilon_1}^{RANS}$ values as low as 1 and as high as 1.81 were used by researchers in various investigations with the corresponding $C_{\varepsilon_2}^{RANS}$ values ranging from 1.8 to 2 [40, 21]. Dynamic coefficient formulations were also proposed by some researchers [45, 46, 35, 34, 41, 42]. Several strategies were investigated for the setting of the RANS model coefficients during the course of this work. In the current implementation, for $C_{\varepsilon_1}^{RANS}$, we use the static value of 1.35 as recommended by Chien [8] for wall-bounded flows and employ the following dynamic formulation for $C_{\varepsilon_2}^{RANS}$ proposed by Merci et al. [35]

$$C_{\varepsilon_2}^{RANS} = \frac{11}{6} + \frac{0.075\Omega T_t}{1 + S^2 T_t^2} \tag{42}$$

where

$$S = (2S_{ij}S_{ij})^{1/2}, \quad \Omega = (2\Omega_{ij}\Omega_{ij})^{1/2}, \quad S_{ij} = \frac{1}{2}\left(\frac{\partial U_i}{\partial x_j} + \frac{\partial U_j}{\partial x_i}\right), \quad \Omega_{ij} = \frac{1}{2}\left(\frac{\partial U_i}{\partial x_j} - \frac{\partial U_j}{\partial x_i}\right) \tag{43}$$

and T_t is the time scale introduced earlier. The values of the turbulent diffusion coefficients σ_K and σ_ε are set to 1 and 1.3, respectively, which are among the commonly used values [40, 21]. We take $\kappa = 0.41$ and $C_\mu = 0.09$ in the computation of S_ε via Eq. (39).

4 Coupling of the RANS and LES Zones

The governing equations solved in the RANS and LES zones are identical but the solution variables naturally have a different meaning between the two zones. The modeled turbulent stresses that appear in the governing equations are combined linearly as follows, using the blending function proposed by Abe [1]

$$\tau_{ij} = f_b \cdot \tau_{ij}^{LES} + (1 - f_b) \cdot \tau_{ij}^{RANS} \tag{44}$$

where

$$f_b = 1 - \exp\left[-\left(\frac{d}{C_b \cdot \Delta}\right)^{\alpha}\right], \quad \Delta = \max(\Delta_1, \Delta_2, \Delta_3) , \tag{45}$$

Δ_i denotes the grid spacing along the three directions of a structured grid and d is the wall-normal distance. For an unstructured grid, the above relation for Δ is not normally applicable and an alternate definition such as the cubic-root of the cell volume can be used. C_b and α are free parameters that determine the blending function shape and the near-wall extent of the RANS zone. Following Abe [1], the α parameter which controls the sharpness of f_b is set to 6. This value can be taken as a universal constant. For the two test cases considered in this study, the maximum wall-parallel grid spacing is on the order of 100 wall units in the attached flow regions. Simulations indicate that $C_b = 2$ is a reasonable choice for both test cases as it allows the hybrid simulation to become a full LES beyond about 200 units in the wall-normal direction. This puts the transition between the RANS and LES zones within the logarithmic layer in the attached flow regions. The C_b parameter may require adjustment with very different maximum wall-parallel grid spacings so that the switch from RANS to LES does not happen suboptimally. Too early a switch could result in LES being performed on a poor grid resolution in the near-wall region while too late a switch could potentially lead to RANS being performed on a grid resolution that could have been used for LES instead. In the two transport equations, the production and destruction terms as well as the quantities in the modeled turbulent diffusion terms (i.e., $\mu_t/\sigma_{\varepsilon_{sgs}}$ and $\sigma_\varepsilon^{-1}\mu_t^{RANS}$ for the total/subgrid viscous dissipation and the analogous terms for the total/subgrid turbulent kinetic energy) are blended linearly in a similar fashion to Eq. (44). The blending of the source term S_ε is also similar, with its value set to zero in the LES region. The blended quantities are used in the time integration of the transport equations.

Fröhlich and von Terzi [15] noted that the linear blending of RANS and LES models as in Eq. (44) can lead to the generation of unphysical flow structures in the transition region. Evidence of any such unphysical structures would be present in the statistical results. As will be seen, the present HRLES method produces a generally smooth transition in the mean velocity and turbulent shear stress profiles between the RANS and LES zones. However, some excess turbulent kinetic energy within the transition region and parts of the RANS zone can be present at certain locations in the flow. This is likely an artifact of the blending, but it could also be related to the unsteadiness in the LES zone bleeding toward the RANS zone. The backscatter generated by the present SGS model appears to mitigate the effects of any spurious phenomena as it helps break down the large-scale structures in the transition region between the RANS and LES zone. This is supported by the fact that no adverse impact of the blending is found on the mean velocity and turbulent shear stress profiles.

5 Specification of the Boundary Conditions for Transport Equation Variables

We now discuss the boundary conditions for the transport equation variables, K or k_{sgs} and ε or ε_{sgs}. At the viscous solid wall where RANS is active, $K = 0$ while dissipation is balanced by viscous diffusion, which then leads to the following boundary condition for ε

$$\varepsilon = \nu_w \frac{\partial^2 K}{\partial x_j^2}\bigg|_{wall} \tag{46}$$

where ν_w is the kinematic viscosity at the wall. In this work, the following more computationally robust form, which is equivalent to the above identity based on the asymptotic behavior of K and ε very near the wall, as shown by Jones and Launder [22], is used instead

$$\varepsilon = 2\nu_w \left(\frac{\partial \sqrt{K}}{\partial x_j}\right)^2 \bigg|_{wall} . \tag{47}$$

At an outer freestream or inviscid solid wall boundary where LES is active, $k_{sgs} = 0$ and $\varepsilon_{sgs} = 0$.

The transport equations are solved without any modifications at the outflow boundary. At the domain inlet, a rescaling-recycling technique described in Uzun and Malik [62, 63, 65] is applied to generate an incoming turbulent boundary layer. The method originally developed for WRLES/DNS applications has been modified to include the recycling of the transport equation variables. The present inflow generation procedure is applicable to problems with a periodic spanwise direction. Application to problems without a periodic spanwise direction would require some changes to the method. Assuming spanwise periodicity, the transport quantities in the RANS region extracted from the recycle plane are rescaled and reintroduced at the inlet plane as follows

$$K(x_{\text{inlet}}, y, z, t) = K(x_{\text{recycle}}, y\delta_{\text{recycle}}/\delta_{\text{inlet}}, z + \Delta z, t - \Delta t) \left(\frac{u^*_{\text{inlet}}}{u^*_{\text{recycle}}} \right)^2 , \tag{48}$$

$$\varepsilon(x_{\text{inlet}}, y, z, t) = \varepsilon(x_{\text{recycle}}, y\delta_{\text{recycle}}/\delta_{\text{inlet}}, z + \Delta z, t - \Delta t) \left(\frac{u^*_{\text{inlet}}}{u^*_{\text{recycle}}} \right)^4 \left(\frac{\nu_{\text{recycle}}}{\nu_{\text{inlet}}} \right) . \tag{49}$$

Analogous expressions apply for the rescaling and recycling of k_{sgs} and ε_{sgs} in the LES region. Here, x, y, z represent, respectively, the local streamwise, wall-normal and periodic spanwise directions, with $y = 0$ corresponding to the wall location, u^* is the wall friction velocity and ν is the wall kinematic viscosity. The transport variables imposed at the time level, t, are taken from the previous time step level, $t - \Delta t$. A spanwise shift of Δz, also applied in the original method reported in [62, 63, 65], is introduced to suppress the formation of a strong coherence between the inlet and recycle stations. The distance between the inlet and recycle stations, $(x_{\text{recycle}} - x_{\text{inlet}})$, is typically chosen as $10 - 20$ times the incoming boundary layer thickness, δ_{inlet}. The recycle plane boundary layer thickness, δ_{recycle}, is determined dynamically from the running time average of the mean recycle plane profile. The above expressions show that the variables introduced at the inlet plane at the normalized wall distance of y/δ_{inlet} are extracted from the recycle plane at the wall distance of $y\delta_{\text{recycle}}/\delta_{\text{inlet}}$. Normalizing $y\delta_{\text{recycle}}/\delta_{\text{inlet}}$ by δ_{recycle} produces the same relative position as that for the corresponding inlet plane point. The above expressions are derived by assuming that the transport variables in wall units at a given relative position within the boundary layer (i.e. y/δ) have the same value between the inlet and recycle stations.

6 Computational Methodology

The code used in this study solves the unsteady three-dimensional compressible Navier-Stokes equations discretized on multiblock structured and overset grids. For the two test cases, single-block grids are used because of the relatively simple geometries. An optimized prefactored fourth-order accurate compact finite-difference scheme [4] is used to compute all spatial derivatives in the governing equations. This optimized scheme offers improved dispersion characteristics compared to the standard sixth- and eighth-order compact schemes [28]. It is derived from the standard eighth-order compact scheme that has been shown to possess "spectral-like" resolution [28]. Third-order one-sided and biased schemes, respectively, are used on a boundary point and on the point next to the boundary. To eliminate the spurious high-frequency numerical oscillations that may arise from several sources and ensure numerical stability, the present simulations use the tenth-order compact filtering scheme [16], [67], with matching one-sided biased formulations near the physical boundaries. A Beam-Warming type approximately factorized implicit scheme with subiterations is used for the time advancement [12]. More details of the simulation methodology can be found in the publications by Uzun and coworkers [60, 57, 58, 59, 61].

7 First Test Case: Spanwise-Periodic Flow over the Speed Bump

The first test case chosen for the evaluation of the hybrid methodology is the flow past a Gaussian bump (also known as the speed bump) for which comparison data from a high-fidelity simulation by Uzun and Malik [65] is available, which is referred to as the DNS in the results presented below. The spanwise-periodic configuration of the speed-bump flow assumes a uniform two-dimensional profile along the span, which is described by $y(x) = h \exp\left(-(x/x_0)^2\right)$, where $x_0 = 0.195L$, x and y denote the axial and vertical directions, respectively (with z being the spanwise direction), $h = 0.085L$ is the bump height and L is the bump length that is taken as the reference length scale. As depicted in Figure 1, the main features of the problem include the strong favorable pressure gradient (FPG) over the windward side of the bump that generates a substantial acceleration of the incoming flow toward the bump apex and the strong APG over the leeward side that leads to flow separation at a sufficiently high Reynolds number.

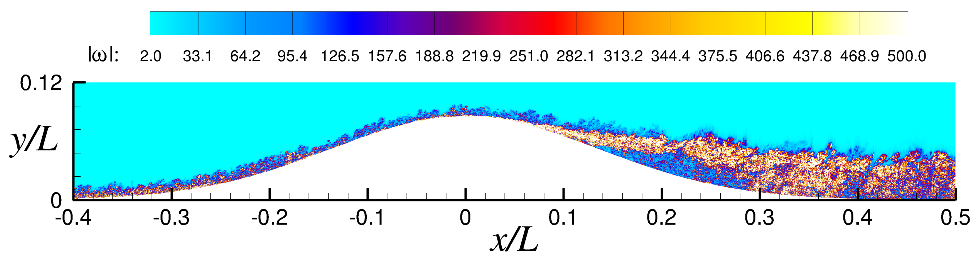

Figure 1. DNS visualization of the flow separation over the leeward side of the Gaussian bump. Contours denote the instantaneous normalized total vorticity magnitude on an $x - y$ plane.

7.1 Simulation Details

The simulation parameters and the computational domain setup are identical to those in the DNS [65]. The Reynolds number based on the upstream reference velocity, U_∞, and L is $Re_L = 2$ million. The corresponding Reynolds number based on h is 1.7×10^5 while the freestream Mach number is 0.2. The mean inflow boundary-layer thickness is $\delta_{in} \approx 0.0055L$, giving $\delta/h \approx 0.065$. The corresponding inflow momentum-thickness Reynolds number is $Re_\theta \approx 1035$. The periodic domain span is set to $0.08L$. A schematic of the computational domain is shown in Figure 2. The domain inflow boundary is at $x/L = -0.8$ while the outflow boundary is at $x/L = 2$. The physical domain ends at $x/L = 1$. The region from $x/L = 1$ to 2 is the sponge zone, in which rapid grid stretching is applied along the streamwise direction. This zone contains a negligible number of points compared to the physical domain because of the significant grid stretching applied. The sponge zone dampens the turbulence in the flowfield before it reaches the outflow boundary, where standard characteristic outflow boundary conditions are applied. Viscous isothermal boundary conditions are imposed on the lower boundary, which contains the speed bump profile. The uniform wall temperature is set the same as the reference freestream value. The outer boundary in the vertical direction is placed at $y/L = 1$, on which a nonreflecting characteristic boundary condition is imposed.

The grid used for the HRLES is extracted from the DNS grid, the details of which are available in Uzun and Malik [65]. To generate the HRLES grid, the DNS grid is coarsened by a factor of 8 along the streamwise direction in much of the computational domain except very near the inflow plane, where the streamwise spacing is kept the same as that in the DNS grid over a short region to enable the proper injection of the incoming turbulent fluctuations by the inflow generation technique. The uniform spanwise spacing of the HRLES grid is nearly 20 times coarser than that of the DNS grid in the entire domain. The maximum wall-parallel spacings in the attached flow sections are around 100 wall units. It should be remarked that in pure RANS calculations, the maximum wall-parallel grid spacings in wall units can be in the thousands.

The coarsening factors applied to the DNS grid to extract the HRLES grid are based on the assumption that a maximum wall-parallel spacing of about 100 units would be a reasonable resolution in the attached flow sections. As the RANS equations are integrated down to the wall, the wall-normal spacings near the wall are kept similar to those in the DNS but the total number of grid points along the wall-normal direction is smaller by a factor of about 2.3 relative to the DNS because of the grid stretching applied away from the wall. The wall-normal spacing on the wall in the attached flow sections is less than or equal to 1 wall unit. The HRLES grid contains about 29 million points in comparison to the 10.2 billion points for the DNS.

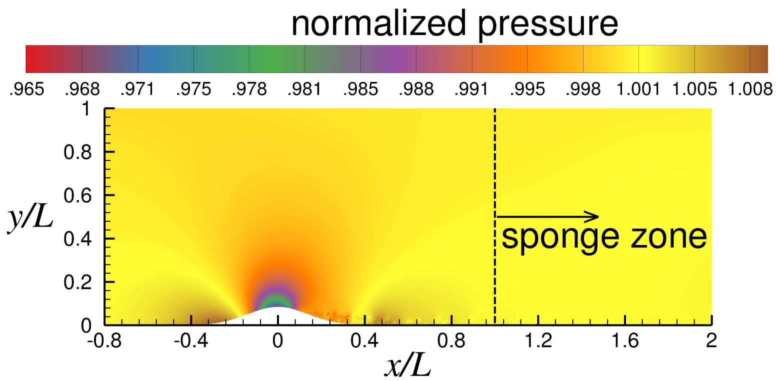

Figure 2. Computational domain schematic. Contours denote the instantaneous pressure normalized by the reference value.

The second-order accurate implicit Beam-Warming scheme [12] is used for the time integration with four subiterations applied per time step. The time step taken in the HRLES is six times the value used in the DNS [65]. The chosen time step corresponds to a maximum Courant-Friedrichs-Lewy (CFL) number of about 30 based on the sum of the acoustic speed and the local flow velocity. This CFL value is close to the stability limit of the implicit time advancement scheme in unsteady simulations. It takes nearly $30,000$ time steps to compute a time interval of L/U_∞. The solution is filtered at every time step using the tenth-order compact filter with a filtering parameter of $\alpha_f = 0.49$ [16], [67]. The procedures used for the turbulent inflow generation were described previously. The mean flow imposed at the inflow boundary is taken from a RANS calculation performed with the low-Reynolds-number correction version of the Spalart-Allmaras model [56]. To reiterate, the mean inflow boundary-layer thickness at $x/L = -0.8$ is $\delta_{in} \approx 0.0055L$. The same mean inflow profile was also used in the DNS [65]. The distance between the inflow and recycle planes is about $12\delta_{in}$. The statistical results in both the HRLES and the DNS were time averaged over about $20L/U_\infty$.

7.2 Results

We now examine the HRLES predictions for the speed-bump flow and make comparisons with the corresponding DNS results [65]. Figure 3 provides the surface pressure coefficient, C_p, and the skin-friction coefficient, C_f, distribution comparisons between the two simulations. These coefficients are given by

$$C_p = \frac{\langle p \rangle - p_\infty}{\frac{1}{2}\rho_\infty U_\infty^2} \quad \text{and} \quad C_f = \frac{\langle \tau_w \rangle}{\frac{1}{2}\rho_\infty U_\infty^2} \tag{50}$$

where ρ_∞, p_∞, U_∞, respectively, are the reference freestream density, pressure and velocity, $\langle p \rangle$ is the mean surface pressure and $\langle \tau_w \rangle$ is the mean wall shear stress. Figure 3 shows a reasonable overall agreement with some notable differences between the two simulations. The C_p plot indicates that the incoming boundary layer encounters an initially mild APG that becomes progressively stronger as the flow approaches the bump foot. The pressure gradient becomes strongly favorable starting at $x/L \approx -0.29$ until very near the bump apex. The strong FPG is responsible for the substantial flow acceleration toward the bump apex, which steepens the mean streamwise velocity gradient adjacent to the wall and causes nearly a fourfold increase in the surface skin friction between the start and the end of the acceleration region. This phenomenon is captured well in the HRLES. As will be seen, the acceleration due to the strong FPG increases the boundary-layer edge velocity to a value of around $1.4U_\infty$ at the bump apex. The strong APG encountered immediately past the bump apex leads to the onset of separation at $x/L \approx 0.1$ in both simulations. In the HRLES, the C_f magnitudes in the separation region are seen to be slightly higher relative to the DNS, indicating a bit stronger reversed flow there while the HRLES C_f magnitudes within the recovery region downstream of the flow reattachment point are lower relative to the DNS. The C_p distributions show some related differences between the two simulations in the separated region. The C_p peak magnitude of the HRLES is slightly lower than that of the DNS; this is believed to be associated with the differences observed in the separated region. The separated flow reattachment point is at $x/L \approx 0.427$ and 0.431 for the DNS and the HRLES, respectively. The corresponding difference in the separation bubble size is only about 1.22%.

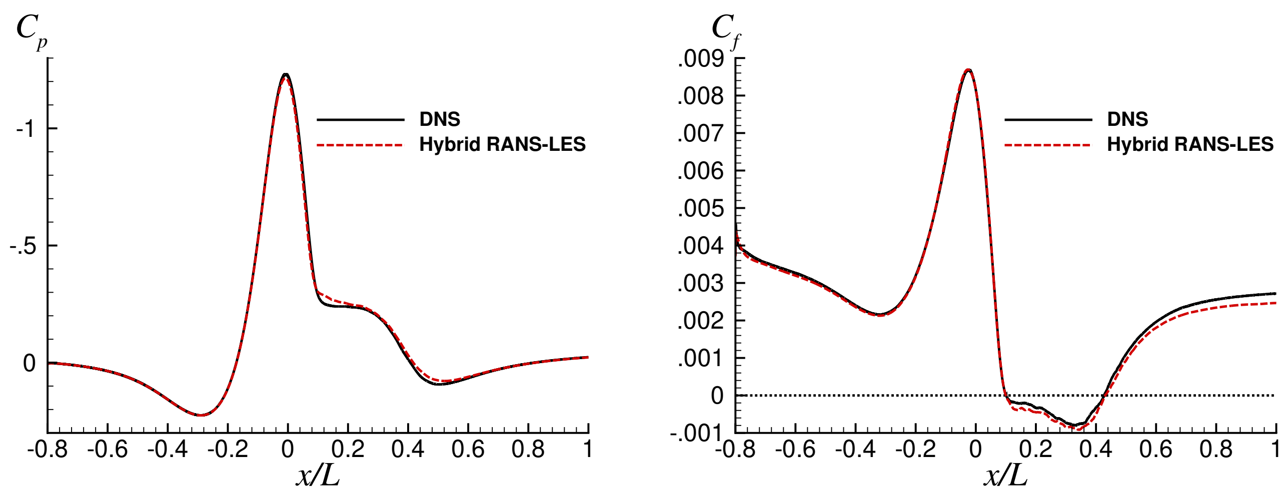

Figure 3. Surface pressure coefficient, C_p, and skin-friction coefficient, C_f, distributions.

The evolution of the time- and spanwise-averaged mean streamwise velocity, U/U_∞, profiles at six evenly-spaced stations over the bump windward side is depicted in Figure 4 while Figure 5 provides the same profiles in terms of wall units. The corresponding turbulent shear stress, $-\langle u'v' \rangle/U_\infty^2$, and turbulent kinetic energy, TKE $= 0.5\left(\langle u'u' \rangle + \langle v'v' \rangle + \langle w'w' \rangle\right)/U_\infty^2$ profiles at the same stations are plotted in Figures 6 and 7, respectively. Here, $\langle u'u' \rangle$, $\langle v'v' \rangle$, and $\langle w'w' \rangle$, respectively, are the streamwise, wall-normal and spanwise components of the turbulent stress in the local wall-normal (or orthogonal) coordinate system at a given station[‡] and the $\langle\ \rangle$ operator denotes averaging in time and along the span. The turbulent shear stress and the mean streamwise velocity are also defined with respect to the local orthogonal system. The six stations cover the region from the bump foot at $x/L = -0.5$ till the bump apex at $x/L = 0$. The first two stations are positioned within the initial APG section identified above while the third station is located near the end of this section and the start of the strong FPG section. The fourth and fifth stations are positioned within the strong FPG section and the sixth station is located at the bump apex and slightly downstream of the end of the strong FPG section. In Figures 4, 6 and 7, the normalized wall-normal distance, n/L, is plotted in

[‡]For this analysis, the mean velocity and turbulent stress components originally defined in the Cartesian coordinate system are first interpolated from the simulation grid onto the local wall-normal line constructed at a given streamwise station. Using the local wall-normal and surface tangent vectors, the interpolated values are then transformed to the corresponding quantities in the local orthogonal coordinate system at a given x/L position on the curved surface.

logarithmic scale. In Figure 5, $n^+ = n u_\tau / \nu_w$, $U^+ = U/u_\tau$, where u_τ is the local friction velocity and ν_w is the kinematic viscosity at the wall. The figures also include the blending function, f_b. To reiterate, the simulation is in full RANS mode when $f_b = 0$, in full LES mode when $f_b = 1$ and in the blended RANS-LES mode when $0 < f_b < 1$. To enable a meaningful comparison with the DNS quantities, the resolved and modeled components of the turbulent shear stress and the TKE are added together in the HRLES and the total quantities are shown.

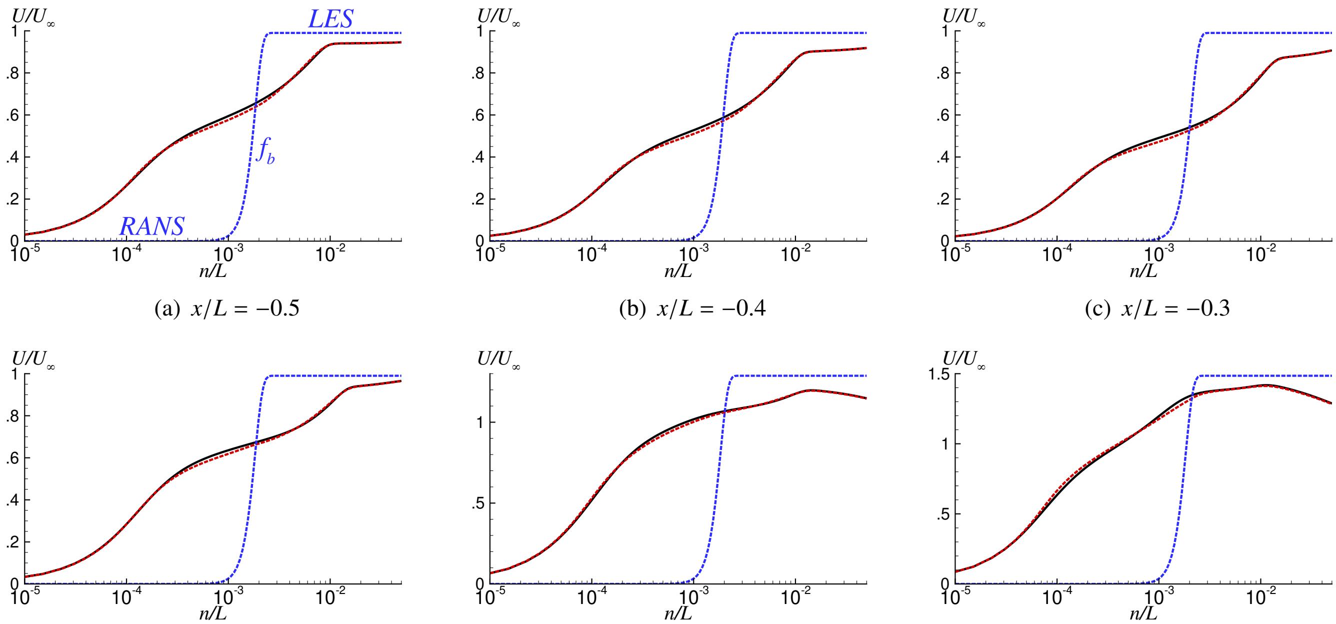

Figure 4. Normalized mean streamwise velocity profiles over the bump windward side. Solid black line denotes the DNS result; dashed red line denotes the HRLES result; dashed blue line indicates the blending function, $0 \leq f_b \leq 1$.

Figures 4 and 5 show that the response of the mean streamwise velocity profile to the adverse and favorable pressure gradients encountered over the bump windward side is captured reasonably well in the HRLES. As seen in Figure 4(f), the acceleration caused by the strong FPG increases the boundary-layer edge velocity to about $1.4U_\infty$ at the bump apex. The profiles in wall units depicted in Figure 5 do not show a logarithmic-layer mismatch as the switch from the RANS calculation to the LES takes place. However, the logarithmic-layer intercept constant of the HRLES mean velocity profile at the first station is slightly lower than that in the DNS, which might be hard to distinguish due to the plot scale. This initial difference in the mean velocity profile convects downstream and appears at the other stations as well. Despite this difference, the overall agreement in the mean velocity profiles over the bump windward side is deemed satisfactory.

The evolutions of the turbulent shear stress profiles over the windward side of the bump depicted in Figure 6 also show a satisfactory overall agreement between the DNS and the HRLES. The reasonably good agreement with the DNS data in the near-wall region covered by RANS shows no indication of modeled-stress depletion [33, 54]. Figure 6 additionally includes the resolved portion of the turbulent shear stress profiles in the HRLES. We observe that the resolved component is nonzero in parts of the RANS zone due to the fact that the unsteadiness originating from the LES zone crosses over into parts of the RANS zone. As seen in the profiles at the first three or four stations, in the early part of the LES zone, there is a considerable difference between the resolved and the total shear stress, indicating a significant contribution from the modeled component. With further distance from the wall, the difference between the total and the resolved shear stress diminishes. It should also be kept in mind that any backscatter generated by the SGS model would energize the resolved motions and thus appear in the form of resolved, rather than modeled, turbulent fluctuations. As the flow moves deeper into the acceleration region and nears the bump apex, the outer region stress levels decay, and the difference between the resolved and the total shear stress in the early part of the LES zone lessens. The two quantities become nearly identical over much of the LES zone at the bump apex, where the outer region stresses are much lower relative to those in the near-wall region.

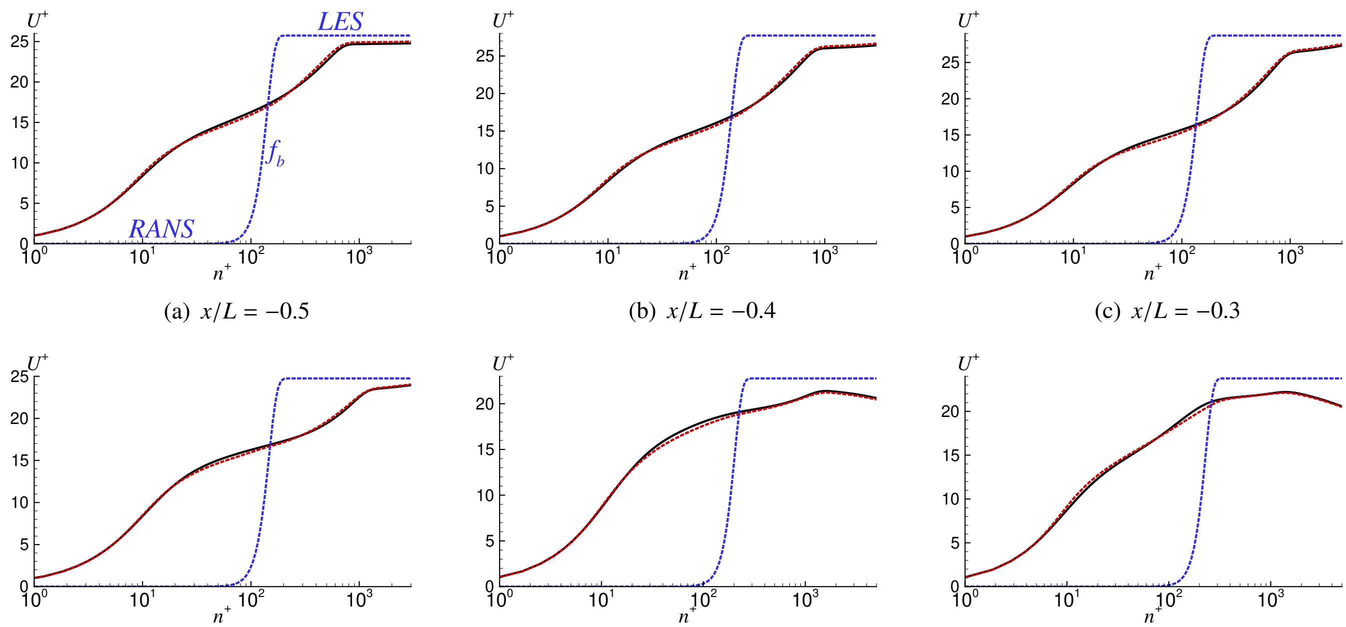

(a) $x/L = -0.5$ (b) $x/L = -0.4$ (c) $x/L = -0.3$

(d) $x/L = -0.2$ (e) $x/L = -0.1$ (f) $x/L = 0$

Figure 5. Mean streamwise velocity profiles in wall units over the bump windward side. Solid black line denotes the DNS result; dashed red line denotes the HRLES result; dashed blue line indicates the blending function, $0 \leq f_b \leq 1$.

The TKE comparisons in Figure 7 reveal that at the first few stations, although a good agreement with the DNS is found very close to the wall and in the outer part of the boundary layer, the intermediate region between the RANS and LES zones contains excess TKE levels, which also appear to cross into parts of the RANS zone. These excess TKE levels might be an artifact of the linear blending of the RANS and LES models [15] but could also be related to the unsteadiness in the LES zone bleeding toward the RANS zone, as noted earlier in Section 4. Yet, this spurious effect does not appear to have any detrimental effect on the mean velocity and turbulent shear stress predictions of the HRLES. As the flow enters the strong FPG region and begins to accelerate, the excess TKE containing portion of the profiles becomes less prominent. Over the latter half of the bump windward side, the TKE profiles show reasonable overall agreement with the DNS despite some observed differences.

As discussed in Uzun and Malik [65], an internal layer develops beneath the accelerated boundary layer over the bump windward side, which is initiated by the switch from the mild adverse to the strong FPG near the bump foot. Since the original peak of the turbulent shear stress is located further away from the wall, the emergence of a strong inner peak close to the wall is one indication of the emerging internal layer. As the flow accelerates, the outer turbulent shear stress peak decays along with the outer region TKE levels as a result of the stabilizing FPG effect there and also that of the convex streamline curvature in the late stages of acceleration toward the apex. These phenomena are duplicated reasonably well by the HRLES when compared to the DNS. However, we observe that the outer peak of the turbulent shear stress and the outer region TKE levels at $x/L = -0.2$ and -0.1 are lower in the HRLES. This likely indicates that an increased LES resolution is needed in the outer part of the accelerated flow for an improved agreement with the DNS. Meanwhile, the original peak of the TKE profile in the incoming boundary layer is positioned close to the wall and falls within the full RANS zone of the HRLES; the near-wall original TKE peak becomes engulfed within the developing internal layer and is further strengthened as the flow acceleration takes place. Despite some differences relative to the DNS, the strengthening of the original TKE peak and the emergence of the near-wall turbulent shear stress peak in the HRLES are captured with reasonable accuracy.

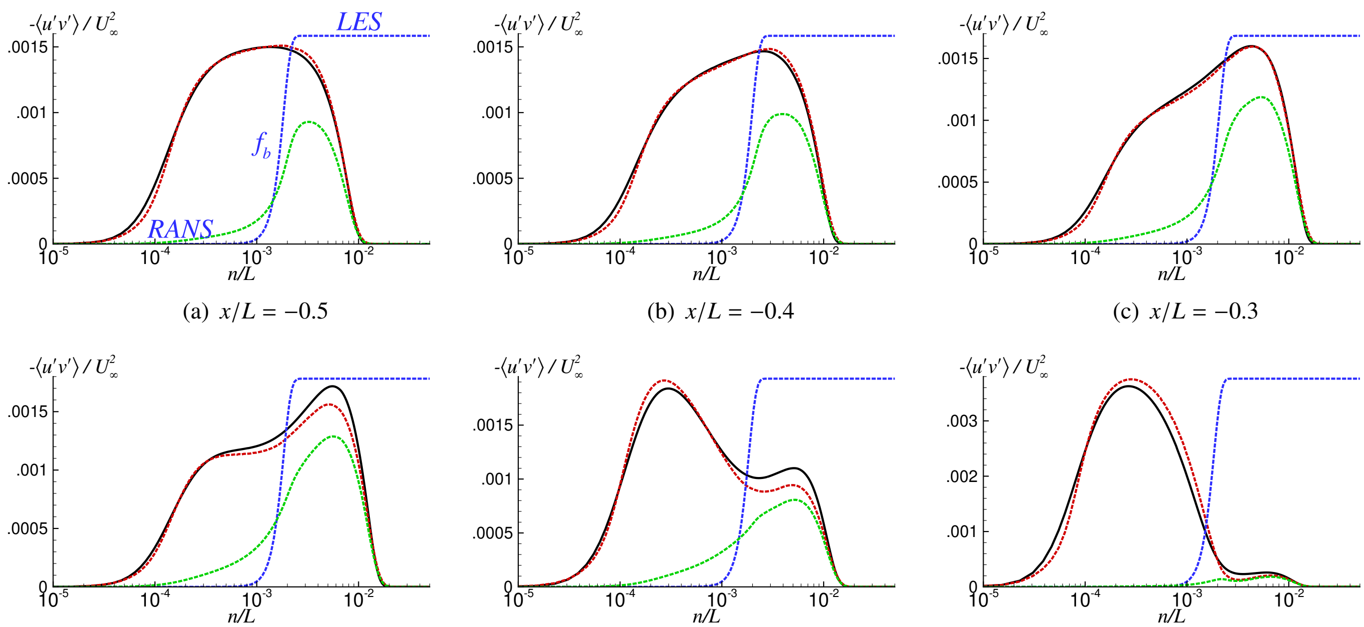

(a) $x/L = -0.5$ (b) $x/L = -0.4$ (c) $x/L = -0.3$

(d) $x/L = -0.2$ (e) $x/L = -0.1$ (f) $x/L = 0$

Figure 6. Normalized total and resolved turbulent shear stress profiles over the bump windward side. Solid black line denotes the DNS result; dashed red line denotes the total value in the HRLES; dashed green line denotes the resolved component in the HRLES; dashed blue line indicates the blending function, $0 \le f_b \le 1$.

Next, we move on to the analysis of the profiles at six stations taken over the bump leeward side, which are positioned at $x/L = 0.05, 0.1, 0.25, 0.4, 0.7$ and 1, respectively, as depicted in Figures 8, 9 and 10. The first station at $x/L = 0.05$ is located about halfway between the bump apex and the flow separation point while the second station at $x/L = 0.1$ is at or very near the flow separation point. The third station at $x/L = 0.25$ is located roughly in the middle of the separated flow region and the fourth station at $x/L = 0.4$ is positioned slightly upstream of the flow reattachment point. The last two stations at $x/L = 0.7$ and 1 are located within the recovery zone. Figure 8(a) shows that as the flow past the bump apex interacts with the strong APG and decelerates toward separation, some differences begin to emerge in the mean velocity profile shapes between the DNS and the HRLES. Associated differences also appear at the second station where the flow is about to detach from the wall, as seen in Figure 8(b). The APG decelerates both the near-wall and outer regions of the boundary layer, and this leads to the formation of an intermediate buffer zone that looks much like a free shear layer, as also seen in Figure 8(b). Once all near-wall momentum has vanished, the flow separation occurs at about the same location in both cases, where $x/L \approx 0.1$. The mean velocity profile shapes in the middle of the separated flow region are quite similar between the two cases, as seen in Figure 8(c), but the reversed flow is a bit stronger in the HRLES, as indicated by the more negative velocities between the wall and the free shear layer. The mean velocity profile shapes near reattachment are also similar, as seen in Figure 8(d), with a relatively stronger reversed flow in the HRLES. Once the separated flow reattaches and the recovery flow begins to develop, we find qualitatively similar mean velocity profile shapes between the two cases, as depicted in Figure 8(e) and 8(f), but there is a noticeable difference in the portion of the velocity profile that corresponds to the logarithmic layer. This discrepancy correlates with the lower C_f predictions in the same region, as seen earlier in Figure 3.

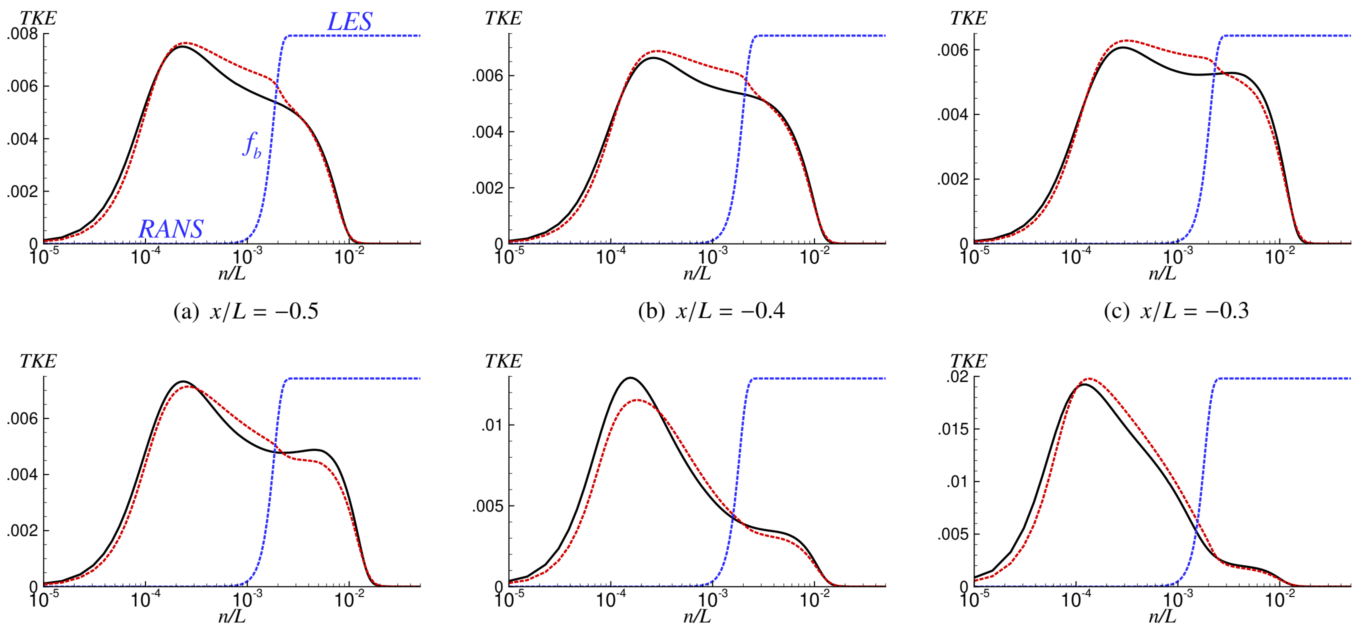

(a) $x/L = -0.5$ (b) $x/L = -0.4$ (c) $x/L = -0.3$

(d) $x/L = -0.2$ (e) $x/L = -0.1$ (f) $x/L = 0$

Figure 7. Normalized total turbulent kinetic energy profiles over the bump windward side. Solid black line denotes the DNS result; dashed red line denotes the HRLES result; dashed blue line indicates the blending function, $0 \leq f_b \leq 1$.

Examination of the turbulent shear stress and the TKE profiles over the bump leeward side, depicted in Figures 9 and 10, shows a reasonable similarity between the DNS and the HRLES at some stations and greater differences at others. The turbulent shear stress and TKE peaks, which are positioned very close to the wall within the internal layer at the bump apex, weaken as the flow decelerates toward separation. This is due to the substantial reduction in the near-wall strain-rate magnitude by the strong APG, which then turns off the production of turbulence in the vicinity of the wall by the time the flow separates. We also observe the formation of new outer peaks within the emerging free shear layer, as depicted in Figures 9(b) and 10(b). These phenomena are duplicated with an acceptable level of accuracy in the HRLES. At the separation point, the turbulent shear stress and the TKE profiles show some differences between the DNS and the HRLES, which are related to the mean velocity profile differences at the same station noted earlier. The relative agreement in the middle of the separated region is quite good for both the turbulent shear stress and the TKE, as seen in Figures 9(c) and 10(c). However, differences start to reappear near the point of reattachment, as seen in Figures 9(d) and 10(d). We find lower peaks for both the turbulent shear stress and the TKE within the free shear layer in the HRLES along with the lower TKE levels within the reversed flow region beneath the shear layer. This indicates that the free shear layer and the reversed flow beneath it evolve somewhat differently in the HRLES relative to the DNS. The free shear layer generates energetic eddies, as evidenced by the high TKE levels within the shear layer, that impinge on the wall in the vicinity of the reattachment point. Some of these eddies get diverted into the reversed flow region and move upstream along the wall while the rest get dragged downstream by the recovery flow. Consequently, the peak TKE levels within the free shear layer are correlated with the considerable TKE levels found in the recirculating flow. The rise in the turbulent shear stress within the reversed flow region near the wall is not as prominent as that in the TKE since the wall-normal velocity fluctuations are rather small in that part of the flow.

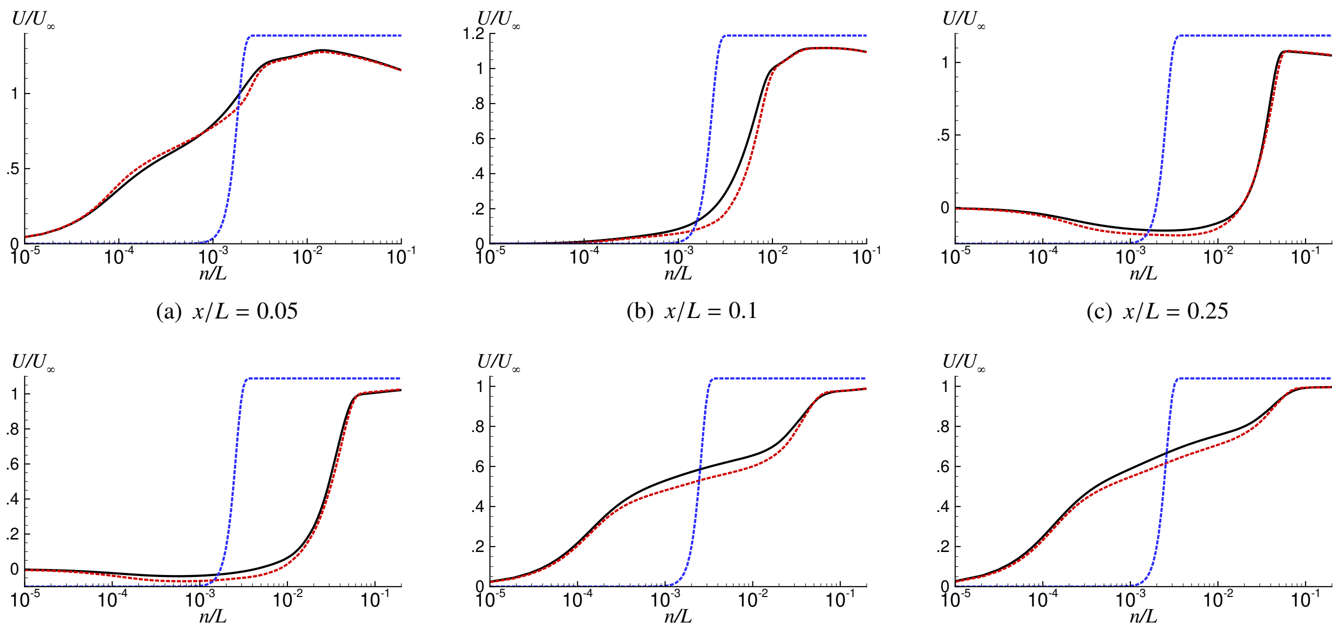

(a) $x/L = 0.05$ (b) $x/L = 0.1$ (c) $x/L = 0.25$

(d) $x/L = 0.4$ (e) $x/L = 0.7$ (f) $x/L = 1$

Figure 8. Normalized mean streamwise velocity profiles over the bump leeward side. Solid black line denotes the DNS result; dashed red line denotes the HRLES result; dashed blue line indicates the blending function, $0 \leq f_b \leq 1$.

The turbulent shear stress profile comparison at $x/L = 0.7$, located in the recovery region, once again shows a good agreement between the DNS and the HRLES despite the relatively lower TKE levels in the HRLES at the same station. As the recovery flow evolves, the initially high near-wall TKE levels, which are found in the vicinity of the reattachment point, decrease as the energetic eddies from the impinging shear layer move along the wall beneath the recovery flow and dissipate. The weakly favorable pressure gradient of the recovery region causes the remnants of the free shear layer to gradually dissipate as the flow moves downstream, as indicated by the corresponding velocity profile shapes in Figure 8. This causes the turbulent shear stress and the TKE peaks within the remnants of the free shear layer to weaken with downstream distance. Those outer peaks would eventually disappear with a sufficiently long domain. Meanwhile, another internal layer begins to emerge near the wall within the recovery flow, as indicated by the formation of a new turbulent shear stress and TKE peak there, without any sign of modeled-stress depletion. As the recovery flow develops further, reasonable similarity is found in the turbulent shear stress and TKE profiles at $x/L = 1$.

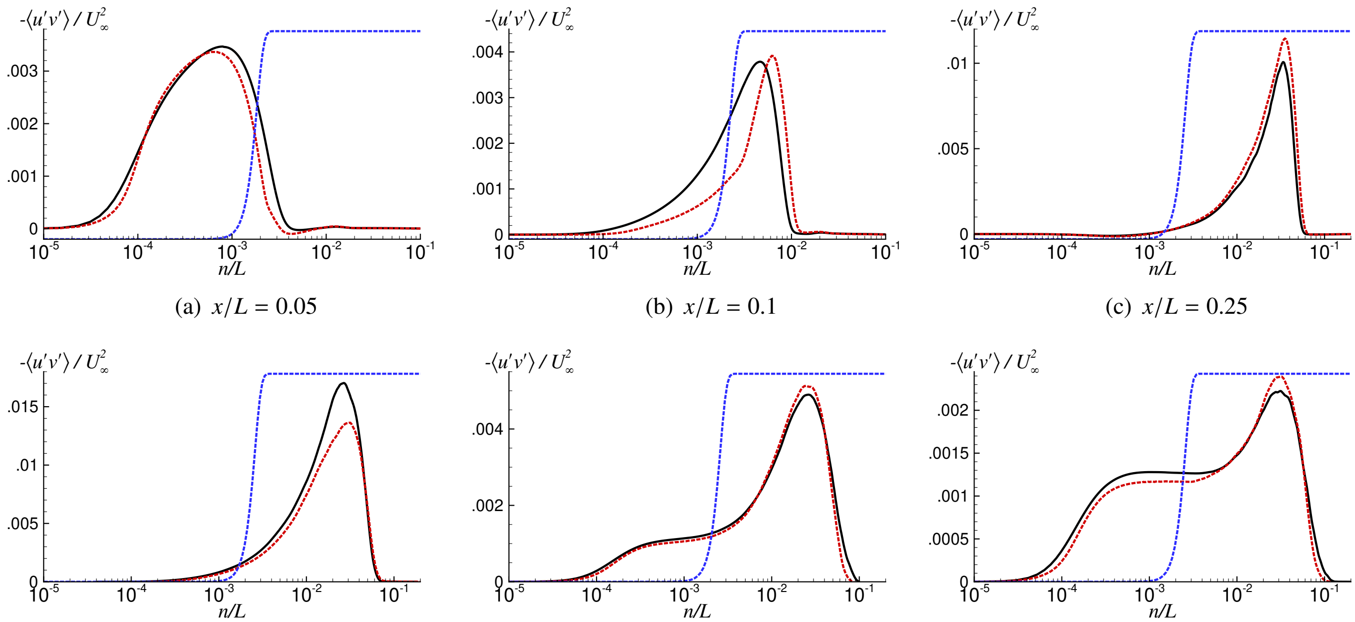

(a) $x/L = 0.05$ (b) $x/L = 0.1$ (c) $x/L = 0.25$

(d) $x/L = 0.4$ (e) $x/L = 0.7$ (f) $x/L = 1$

Figure 9. Normalized total turbulent shear stress profiles over the bump leeward side. Solid black line denotes the DNS result; dashed red line denotes the HRLES result; dashed blue line indicates the blending function, $0 \leq f_b \leq 1$.

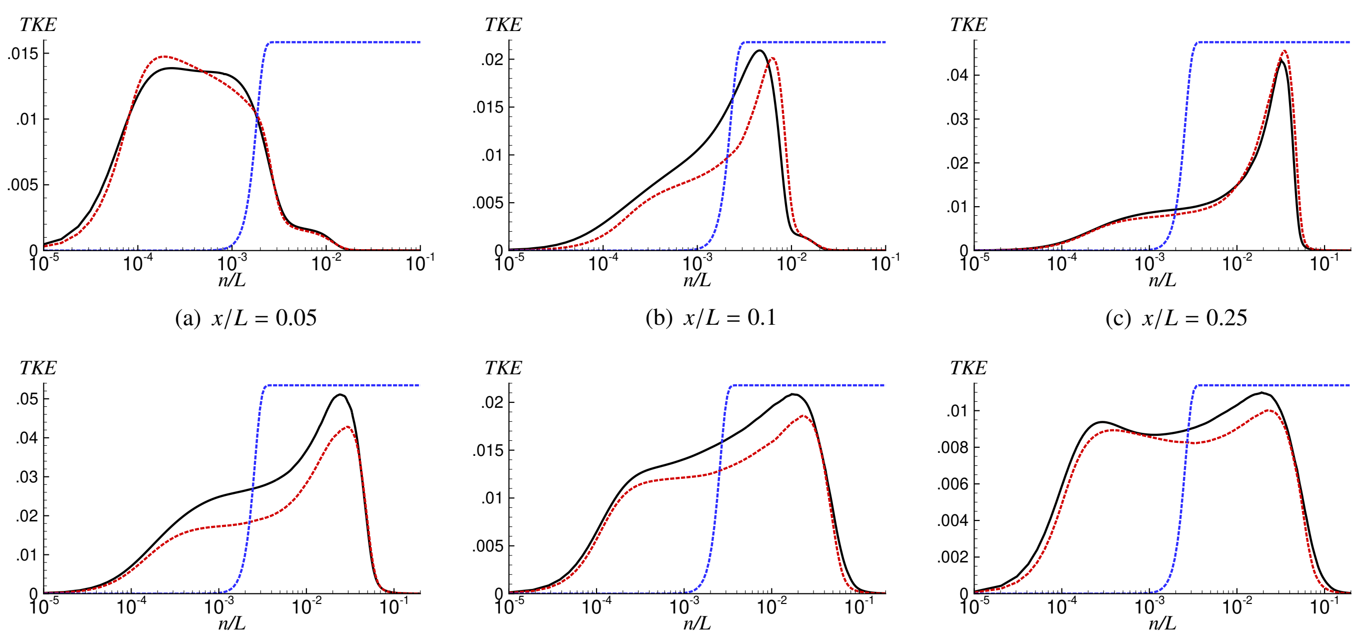

(a) $x/L = 0.05$ (b) $x/L = 0.1$ (c) $x/L = 0.25$

(d) $x/L = 0.4$ (e) $x/L = 0.7$ (f) $x/L = 1$

Figure 10. Normalized total turbulent kinetic energy profiles over the bump leeward side. Solid black line denotes the DNS result; dashed red line denotes the HRLES result; dashed blue line indicates the blending function, $0 \leq f_b \leq 1$.

To summarize the findings, the comparisons with the DNS data show reasonable success for the HRLES in the prediction of the speed-bump flow. Although better agreement with the DNS would be desirable in certain parts of the flow, the comparisons have shown that the main features of the problem are predicted with an acceptable level of accuracy by the HRLES performed using about 29 million grid points as opposed to the 10.2 billion grid points for the DNS. While grid refinement in parts of the flow resolved by LES should provide a better agreement with the DNS for some quantities, improvement of the recovery flow C_f predictions would likely require further enhancements to the RANS model since the accuracy of the near-wall solution strongly depends on the performance of the RANS turbulence model. To reiterate, the maximum wall-parallel spacings within the attached flow sections covered by RANS correspond to around 100 wall units while the wall-normal spacing on the wall is less than or equal to about 1 wall unit. This holds both in the attached flow upstream of separation and the downstream recovery region. With this resolution, the details of the near-wall region upstream of separation are predicted reasonably well by the RANS model. Note that in pure RANS calculations, the maximum wall-parallel grid spacings in wall units can be in the thousands, compared to which the present maximum wall-parallel spacings are considerably finer because the outer region is resolved using LES. These observations suggest that the underprediction of C_f within the recovery region is likely associated with a shortcoming of the RANS turbulence model in this particular region rather than with insufficient grid resolution in the RANS zone.

8 Second Test Case: Spanwise-Periodic Flow over the Smooth Ramp

The second test case chosen for the evaluation of the hybrid methodology is the flow past a smooth ramp for which comparison data from a DNS by Uzun and Malik [66] is available. The smooth ramp profile is described by

$$\frac{y}{L} = \frac{h}{L}\left[1 - 10\left(\frac{x}{L}\right)^3 + 15\left(\frac{x}{L}\right)^4 - 6\left(\frac{x}{L}\right)^5\right] \tag{51}$$

where x, y, z, respectively, denote the axial, vertical and spanwise directions, L is the ramp length that is taken as the reference length scale and $h = 0.22L$ is the ramp height. The ramp profile begins at $(x, y) = (0, h)$ and ends at $(x, y) = (L, 0)$. The sections upstream and downstream of the ramp are straight segments, as seen in Figure 11 that also depicts the flow separation due to the strong APG induced by the ramp profile.

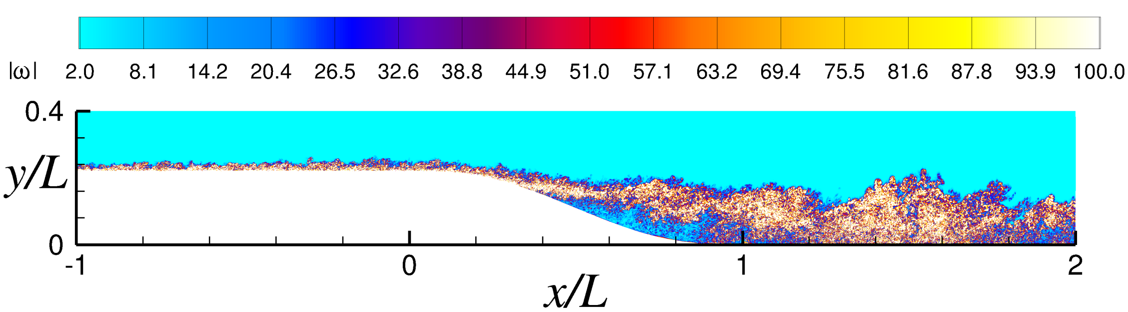

Figure 11. DNS visualization of the APG induced flow separation around the smooth ramp. Contours denote the instantaneous normalized total vorticity magnitude on an $x - y$ plane.

8.1 Simulation Details

The simulation parameters and the computational domain setup are identical to those previously used in the DNS [66]. The Reynolds number based on the inlet reference velocity, U_r, and L is $Re_L = 0.667$ million. The corresponding Reynolds number based on h is about 1.47×10^5. The inlet Mach number is set to 0.2. The incoming boundary-layer thickness is $\delta_{in} = 0.024L$. The corresponding inflow momentum-thickness

Reynolds number is $Re_\theta = 2000$. The periodic domain span is set to $12\delta_{in} = 0.288L$. A schematic of the computational domain is shown in Figure 12. The inflow boundary is at $x/L = -1$ while the outflow boundary is at $x/L = 7$. The physical domain ends at $x/L = 4$. The region from $x/L = 4$ to 7 is the sponge zone, in which the grid is highly stretched in the axial direction. The sponge zone damps out the turbulence before it reaches the outflow boundary, where standard characteristic outflow boundary conditions are applied with a specified back pressure. Viscous adiabatic boundary conditions are imposed on the lower wall that contains the ramp profile. The top boundary is a straight segment placed at $y/L = 0.74$, on which an inviscid wall boundary condition is applied. The imposition of an inviscid top wall makes this an internal flow problem. Hence, the back pressure at the outflow boundary has to be set to 1.013 times the inlet pressure in order to obtain a Mach number of 0.2 at the inlet. This value was determined via precursor WRLES runs performed prior to the DNS [66]. The same back pressure is used in the HRLES.

The grid used for the HRLES is extracted from the DNS grid, the details of which are described in Uzun and Malik [66]. To generate the HRLES grid, the DNS grid is coarsened by a factor of about 10 along the streamwise direction in much of the computational domain except over a short section near the inflow plane, where the streamwise grid spacing is kept the same as that in the DNS grid to enable the proper injection of the incoming turbulent fluctuations by the inflow generation technique. The uniform spanwise spacing of the HRLES grid is about 20 times coarser than that of the DNS grid in the entire domain. As in the speed-bump-flow, the coarsening factors applied to the DNS grid to extract the HRLES grid for the smooth-ramp flow are chosen such that the maximum wall-parallel spacings in the attached flow regions correspond to around 100 wall units. The wall-normal spacings in the vicinity of the lower wall are similar to those in the DNS and the wall-normal spacing on the wall is less than or equal to about 1 wall unit. The total number of grid points along the wall-normal direction is smaller by a factor of about 2.5 relative to the DNS. The HRLES grid contains about 23.6 million points in comparison to the 10.3 billion points for the DNS.

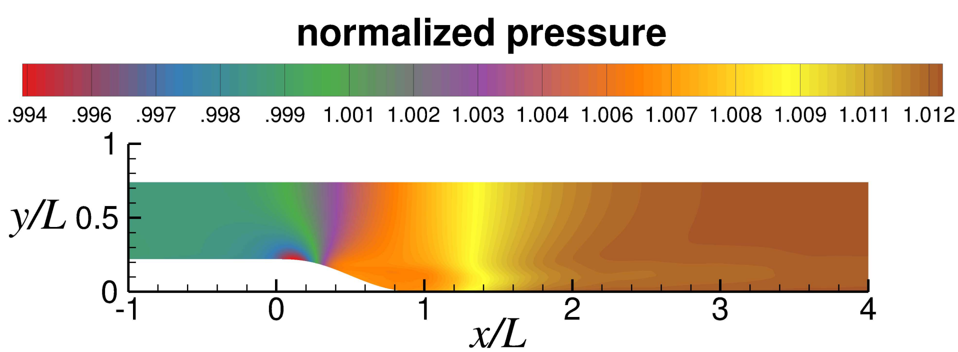

Figure 12. Computational domain schematic. Contours denote the mean pressure normalized by the reference value. Note that the sponge zone downstream of the physical domain is omitted here.

The second-order accurate implicit Beam-Warming scheme [12] is used for the time integration with four subiterations applied per time step. The time step taken in the HRLES is six times the value used in the DNS [66] and corresponds to a maximum CFL number of about 30, which is close to the stability limit of the implicit time advancement scheme. It takes about 8333 time steps to compute a time interval of L/U_r. The solution is filtered at every time step using the tenth-order compact filter [16], [67] with a filtering parameter of $\alpha_f = 0.475$, which is lower than the usual value of 0.49 since $\alpha_f = 0.49$ leads to numerical instability on the present HRLES grid. The DNS was performed with $\alpha_f = 0.49$ [66]. The turbulent inflow generation is based on the same procedures described previously. The mean flow imposed at the inflow boundary is taken from the DNS of Schlatter and Örlü [49] at $Re_\theta = 2000$ for a ZPG turbulent boundary layer. The mean inflow boundary-layer thickness at $x/L = -1$ is $\delta_{in} = 0.024L$. The same mean inflow profile was also used in the DNS [66]. The distance between the inflow and recycle planes is $10\delta_{in}$. The statistical results in both the HRLES and the DNS were time averaged over about $50L/U_r$ as the internal flow nature of the problem required a fairly long averaging interval for the full convergence of the statistics.

8.2 Results

We now examine the HRLES predictions for the smooth-ramp flow and make comparisons with the corresponding DNS results [66]. Figure 13 provides the surface pressure coefficient, C_p, and the skin-friction coefficient, C_f, distribution comparisons on the lower wall. These coefficients are given by

$$C_p = \frac{\langle p \rangle - p_r}{\frac{1}{2}\rho_r U_r^2} \quad \text{and} \quad C_f = \frac{\langle \tau_w \rangle}{\frac{1}{2}\rho_r U_r^2} \tag{52}$$

where ρ_r, p_r, U_r, respectively, are the inlet density, pressure and velocity, which are taken as the reference values, $\langle p \rangle$ is the mean surface pressure and $\langle \tau_w \rangle$ is the mean wall shear stress. Figure 13 shows a reasonable overall agreement with some differences between the two simulations. The incoming boundary layer encounters an initially mild FPG far upstream of the ramp, as indicated by the C_p variation there. The upstream FPG becomes relatively stronger in the vicinity of $x/L = -0.2$ and persists over the early ramp section until $x/L \approx 0.12$. This causes a rise in C_f over that segment. After passing through the FPG region over the early ramp section, the flow encounters the strong APG and begins to slow down. This deceleration leads to the onset of separation at $x/L \approx 0.383$ in the DNS and slightly later at $x/L \approx 0.397$ in the HRLES. We find that the HRLES predicts relatively higher C_f magnitudes in the middle section of the separated region, indicating a stronger reversed flow there. The C_f magnitudes within the downstream recovery region are lower in the HRLES, similar to what was observed in the speed-bump flow. The reattachment point of the separated flow is at $x/L \approx 1.474$ and 1.445 for the DNS and the HRLES, respectively. The corresponding difference in the separation bubble size prediction is about 3.94%. The stronger C_p plateau of the HRLES relative to the DNS, as seen in Figure 13, is believed to be associated with the stronger reversed flow of the HRLES in parts of the separated region.

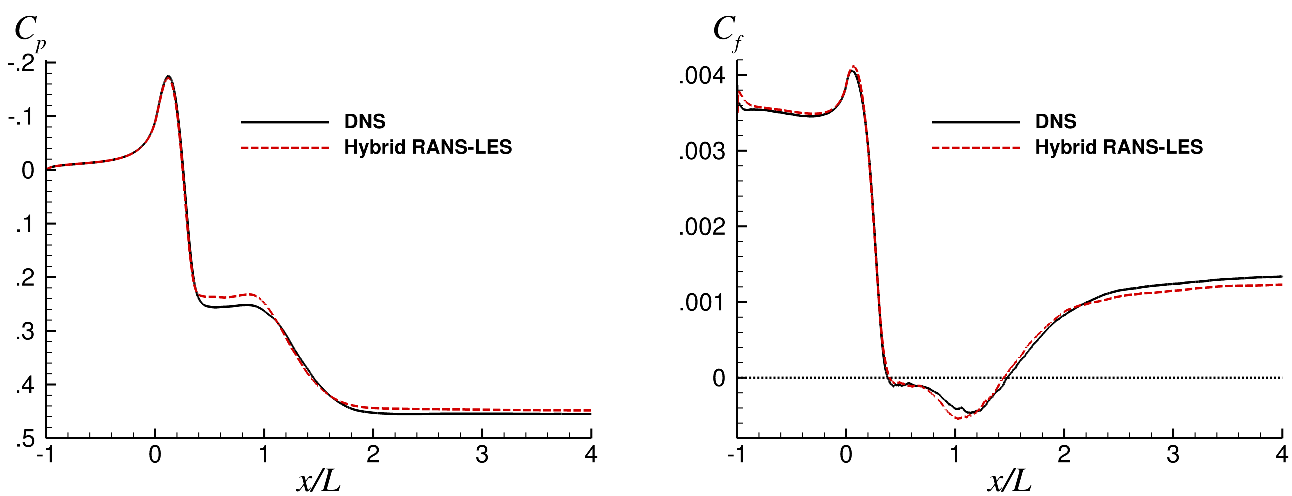

Figure 13. Surface pressure coefficient, C_p, and skin-friction coefficient, C_f, distributions.

The evolution of the time- and spanwise-averaged mean streamwise velocity, U/U_r, total turbulent shear stress, $-\langle u'v' \rangle/U_r^2$, and total turbulent kinetic energy, TKE $= 0.5\left(\langle u'u' \rangle + \langle v'v' \rangle + \langle w'w' \rangle\right)/U_r^2$ profiles at six stations over the region where $-0.6 \leq x/L \leq 0.4$ are depicted in Figures 14, 15 and 16, respectively. Here, $\langle u'u' \rangle$, $\langle v'v' \rangle$, and $\langle w'w' \rangle$, respectively, are the streamwise, wall-normal and spanwise components of turbulent stress in the local orthogonal system at a given station and the $\langle\ \rangle$ operator denotes averaging in time and along the span. The turbulent shear stress and the mean streamwise velocity are also defined with respect to the local orthogonal system. The first station is positioned well upstream of the ramp while the second station is at the start of the ramp. The third station is located near the end of FPG section while the fourth and fifth stations are positioned within the APG section. The sixth station is located slightly downstream of the separation point. The profiles are normalized using U_r. The wall-normal distance from the bump surface, n, is normalized by L and is plotted in logarithmic scale. The figures also include the blending function, f_b.

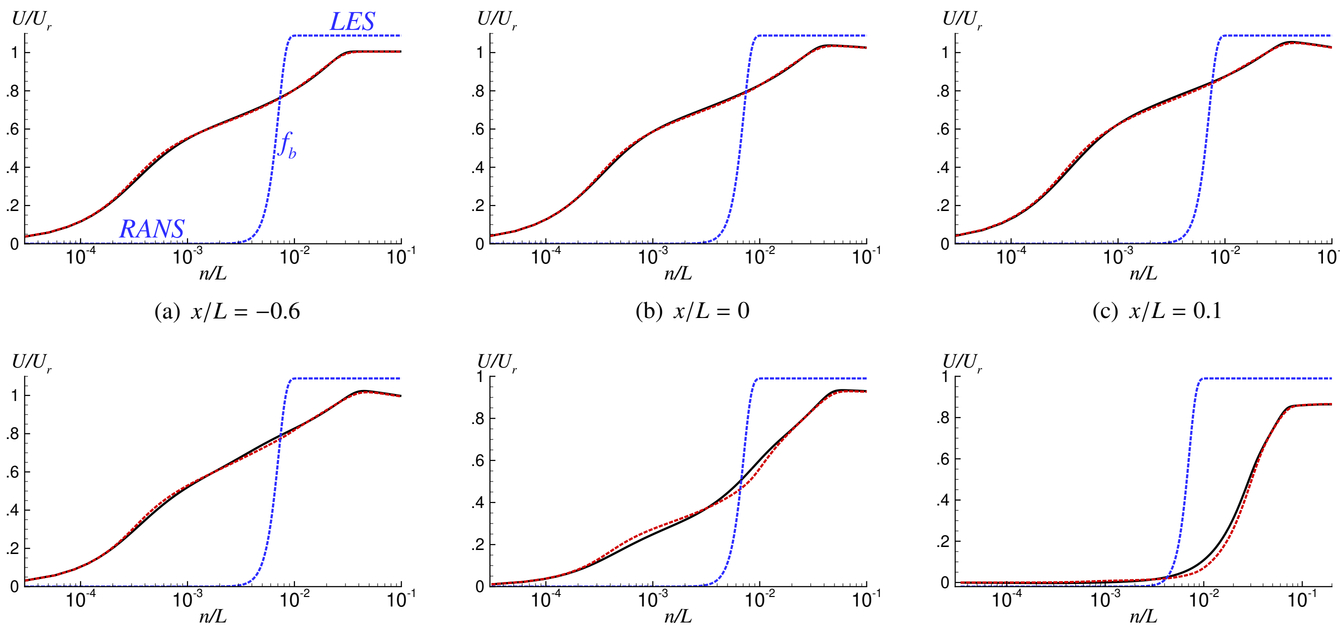

(a) $x/L = -0.6$ (b) $x/L = 0$ (c) $x/L = 0.1$

(d) $x/L = 0.2$ (e) $x/L = 0.3$ (f) $x/L = 0.4$

Figure 14. Normalized mean streamwise velocity profiles where $-0.6 \leq x/L \leq 0.4$. Solid black line denotes the DNS result; dashed red line denotes the HRLES result; dashed blue line indicates the blending function, $0 \leq f_b \leq 1$.

Figure 14 shows very good agreement in the mean velocity profiles at the first three stations located within the FPG region noted above. There is no discontinuity in the portion of the velocity profiles corresponding to the logarithmic layer as the transition from the RANS calculation to the LES takes place. The boundary-layer edge velocity in the accelerated flow due to the FPG sees a modest increase to a value of about $1.055U_r$ at $x/L = 0.1$, which is positioned near the end of the FPG. Some differences begin to emerge between the two simulations once the flow starts interacting with the APG prior to separation. The fourth station positioned in the early stages of the APG still shows a reasonable agreement while the fifth station positioned deeper in the APG shows a more significant difference. These comparisons suggest that the flow deceleration near the wall occurs at a relatively faster pace in the DNS, which then leads to a slightly earlier flow separation relative to the HRLES. At the sixth station where the flow has already separated in both cases, we find similar velocity profile shapes with some differences evident in the initial portion of the free shear layer. The evolutions of the turbulent shear stress and the TKE profiles over the same region, as respectively depicted in Figure 15 and 16, show a reasonable overall agreement over the first four stations and greater differences between the two simulations in the late stages of the APG, which are associated with the mean velocity profile differences at the same locations. The HRLES profiles do not show any indication of modeled-stress depletion. The buildup of excess TKE in the intermediate region between the RANS and

LES zones and its crossover into parts of the RANS zone, first identified in the speed-bump flow analysis, are also present here as can be seen in the first few stations depicted in Figure 16.

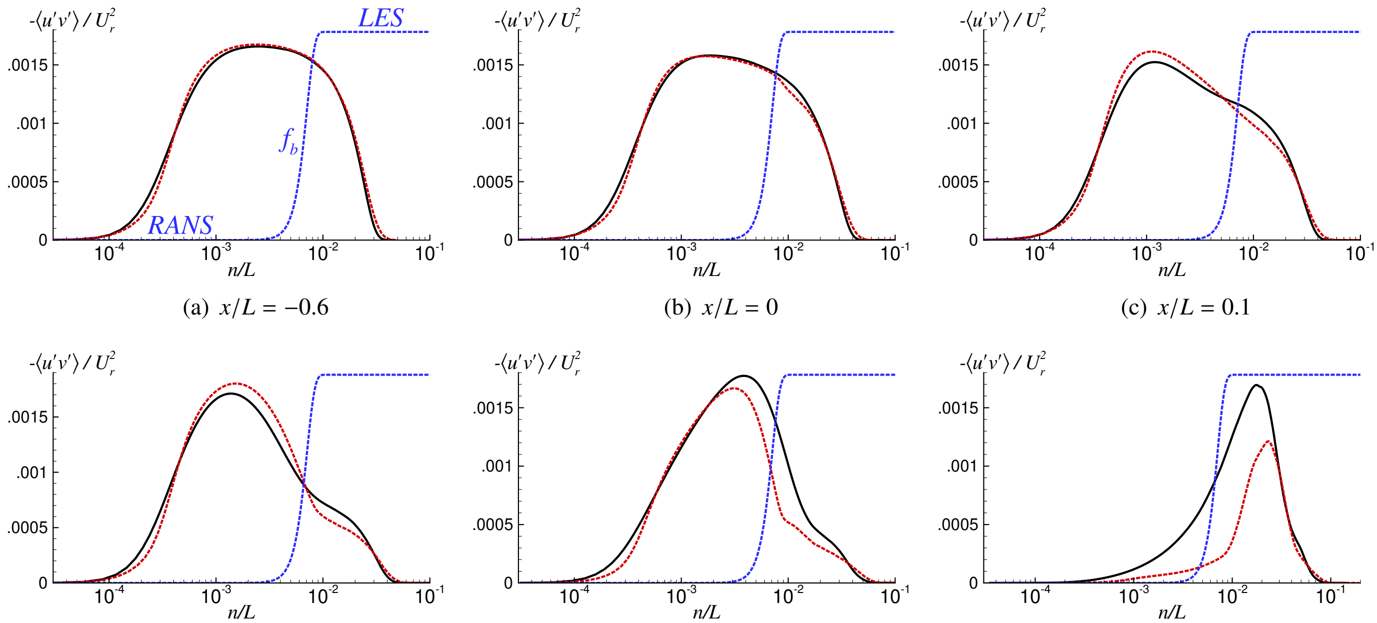

(a) $x/L = -0.6$ (b) $x/L = 0$ (c) $x/L = 0.1$

(d) $x/L = 0.2$ (e) $x/L = 0.3$ (f) $x/L = 0.4$

Figure 15. Normalized total turbulent shear stress profiles where $-0.6 \leq x/L \leq 0.4$. Solid black line denotes the DNS result; dashed red line denotes the HRLES result; dashed blue line indicates the blending function, $0 \leq f_b \leq 1$.

Next, we examine the profile comparisons at six stations that cover the separated flow and the downstream recovery regions. These profiles are positioned at $x/L = 0.8, 1.2, 1.5, 2, 3$ and 4, respectively, as depicted in Figures 17, 18 and 19. The first two stations are located within the separated region, the third station is positioned slightly downstream of the flow reattachment point and the last three stations are located within the recovery zone. The mean velocity profiles depicted in Figure 17 show a reasonable overall agreement with some differences between the two simulations. As seen in Figure 17(a), the reversed part of the separated flow is relatively stronger in the HRLES at $x/L = 0.8$, as also hinted by the C_f comparison examined earlier. The agreement at the station where $x/L = 1.2$, which is positioned in the latter stages of the separated flow, is quite good with some differences reappearing again at $x/L = 1.5$ due to the slightly earlier flow reattachment in the HRLES. Within the recovery flow, the velocity profile shapes are qualitatively similar but there are differences in the portion of the velocity profile corresponding to the logarithmic layer, as also observed in the speed-bump flow. This is consistent with the lower C_f predictions of the HRLES in the same region.

Comparison of the turbulent shear stress and the TKE profiles in Figures 18 and 19 shows a qualitative similarity at some stations and a more quantitative agreement at others. At $x/L = 0.8$, the turbulent shear stress and the TKE peaks are stronger in the HRLES relative to the DNS while the overall agreement is much better at $x/L = 1.2$. This observation suggests that there are differences in the evolution of the free shear layer between the two simulations, which also have some effect on the development of the reversed flow region. Such differences propagate downstream as the separated flow reattaches and the recovery from separation starts. Subsequently, we find relatively weaker turbulent shear stress and TKE peaks at $x/L = 1.5$ and 2 in the HRLES. As the recovery flow develops further, the turbulent shear stress profiles show reasonable quantitative agreement at the last two stations while the TKE profiles still exhibit some differences. Once again, there is no indication of modeled-stress depletion as the recovery flow develops. The differences in the evolution of the free shear layer between the two simulations, which is believed to be responsible for the mixed level of agreement observed here, suggest that further grid refinement within the separated flow region covered by LES would be necessary to obtain an improved agreement with the DNS.

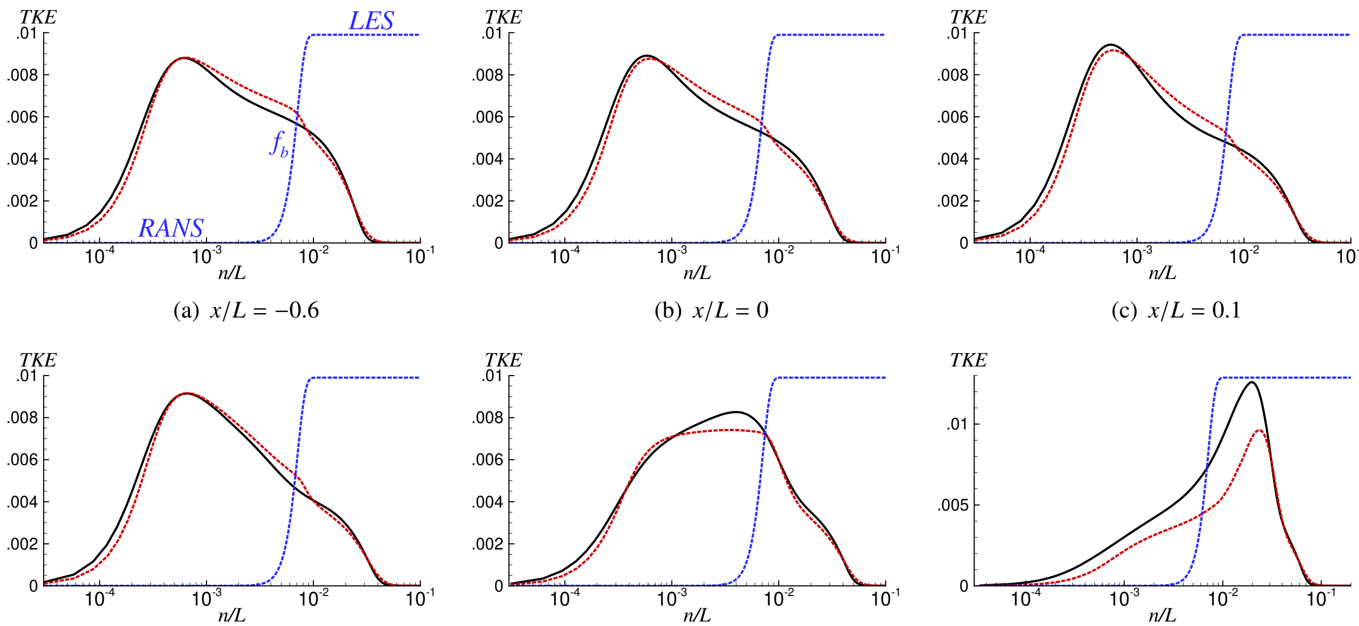

(a) $x/L = -0.6$ (b) $x/L = 0$ (c) $x/L = 0.1$

(d) $x/L = 0.2$ (e) $x/L = 0.3$ (f) $x/L = 0.4$

Figure 16. Normalized total turbulent kinetic energy profiles where $-0.6 \leq x/L \leq 0.4$. Solid black line denotes the DNS result; dashed red line denotes the HRLES result; dashed blue line indicates the blending function, $0 \leq f_b \leq 1$.

To summarize the findings, the analysis of the smooth-ramp flow results and the comparison with the DNS have shown that the main features of the problem are predicted with a reasonable level of accuracy by the HRLES using about 23.6 million grid points as opposed to the 10.3 billion grid points for the DNS. We anticipate that grid refinement in parts of the flow resolved by LES should provide a better agreement with the DNS for some quantities, but the improvement of the recovery flow C_f predictions would likely require further enhancements to the RANS model for an improved representation of the near-wall flow physics in that region. To reiterate, the maximum wall-parallel spacings within the attached flow sections covered by RANS throughout the entire domain correspond to around 100 wall units while the wall-normal spacing on the wall is less than or equal to about 1 wall unit. These spacings are very similar to those used in the speed-bump flow. As in the speed-bump flow, with this level of wall-parallel grid resolution that is considerably finer than those typically used in pure RANS calculations, the details of the near-wall region upstream of separation are also predicted reasonably well by the RANS model in the smooth-ramp flow with similar discrepancies observed in the recovery zone C_f predictions relative to the DNS in both cases. Rectification of the RANS model shortcoming in that particular region remains a subject of future investigations.

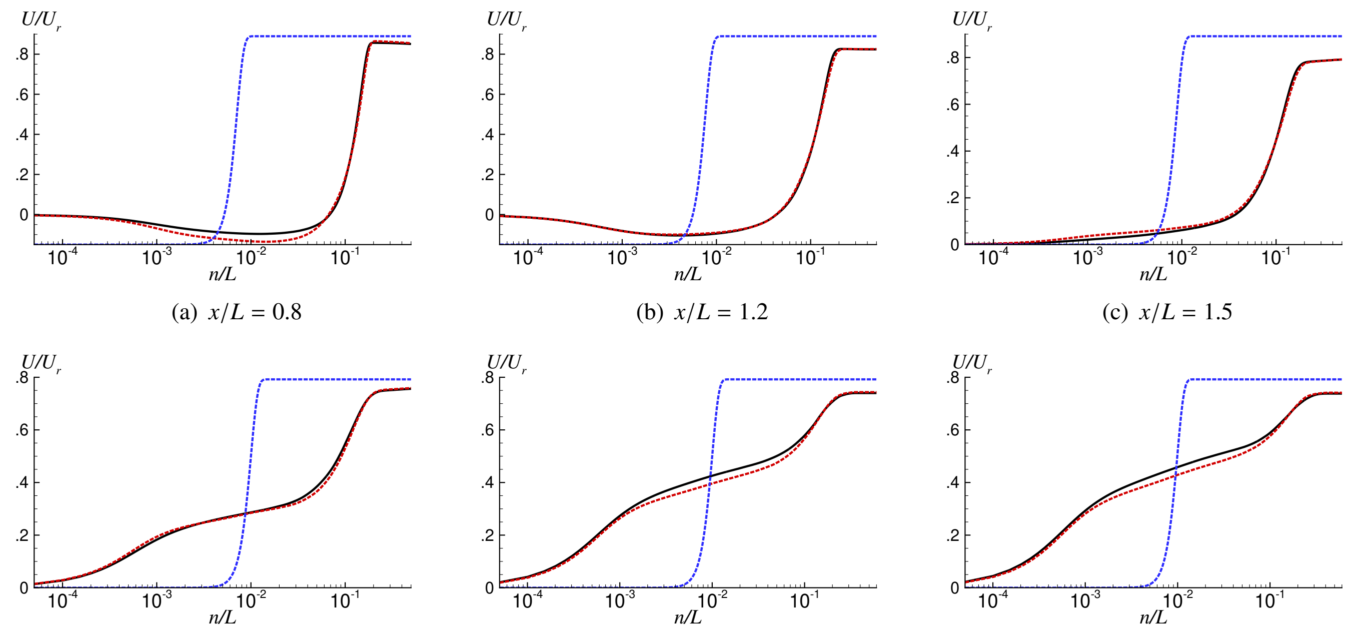

(a) $x/L = 0.8$ (b) $x/L = 1.2$ (c) $x/L = 1.5$

(d) $x/L = 2$ (e) $x/L = 3$ (f) $x/L = 4$

Figure 17. Normalized mean streamwise velocity profiles where $0.8 \leq x/L \leq 4$. Solid black line denotes the DNS result; dashed red line denotes the HRLES result; dashed blue line indicates the blending function, $0 \leq f_b \leq 1$.

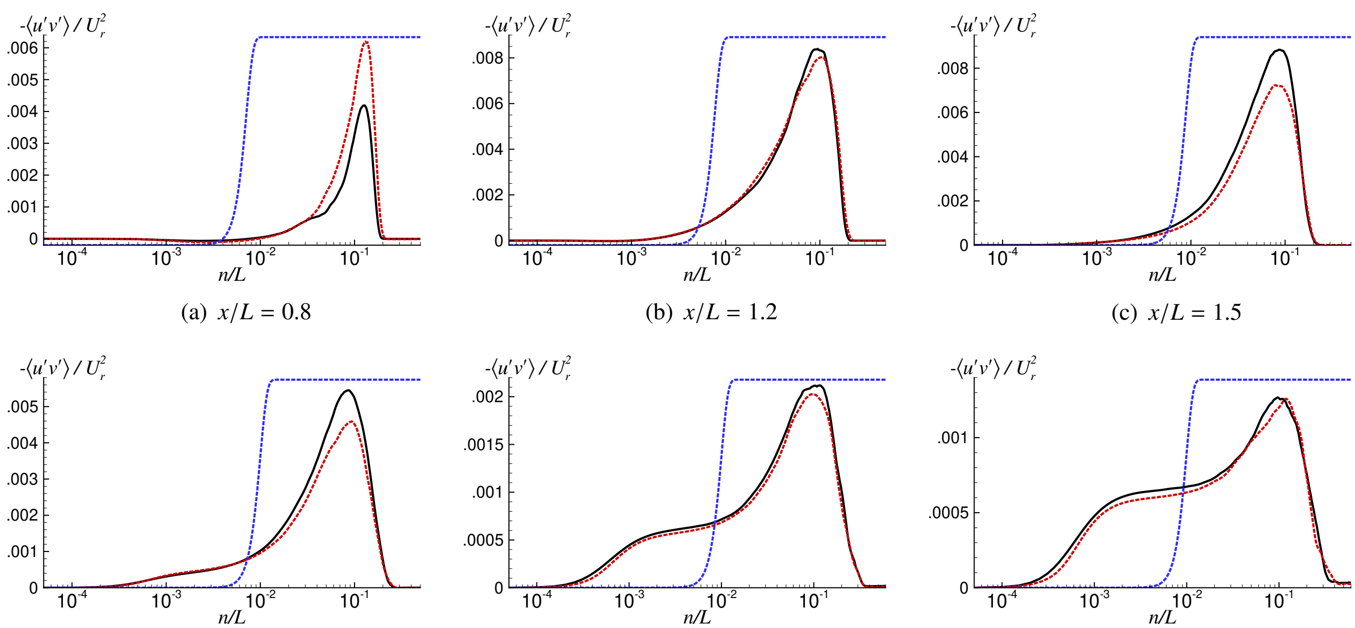

(a) $x/L = 0.8$ (b) $x/L = 1.2$ (c) $x/L = 1.5$

(d) $x/L = 2$ (e) $x/L = 3$ (f) $x/L = 4$

Figure 18. Normalized total turbulent shear stress profiles where $0.8 \leq x/L \leq 4$. Solid black line denotes the DNS result; dashed red line denotes the HRLES result; dashed blue line indicates the blending function, $0 \leq f_b \leq 1$.

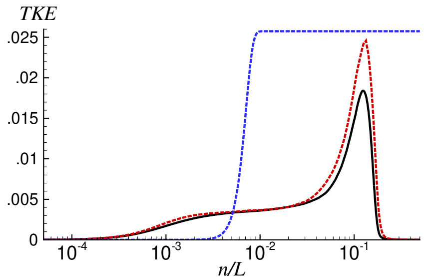

(a) $x/L = 0.8$

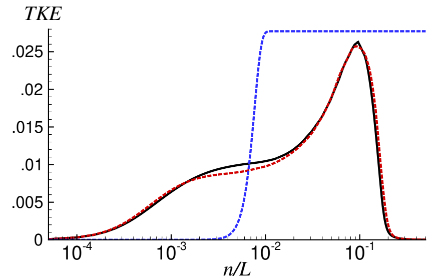

(b) $x/L = 1.2$

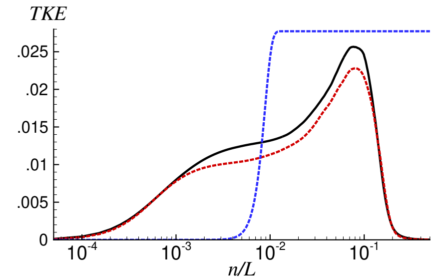

(c) $x/L = 1.5$

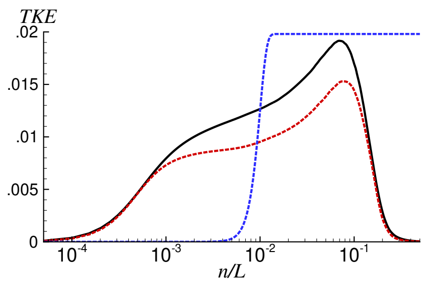

(d) $x/L = 2$

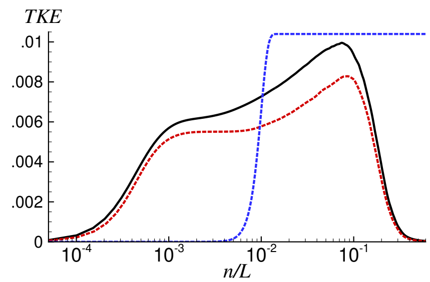

(e) $x/L = 3$

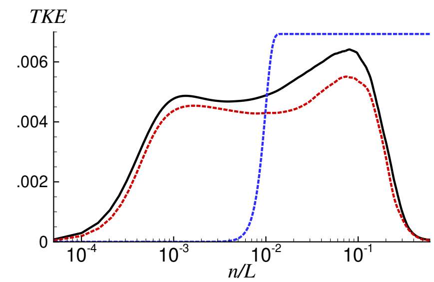

(f) $x/L = 4$

Figure 19. Normalized total turbulent kinetic energy profiles where $0.8 \leq x/L \leq 4$. Solid black line denotes the DNS result; dashed red line denotes the HRLES result; dashed blue line indicates the blending function, $0 \leq f_b \leq 1$.

9 Summary and Concluding Remarks

A zonal hybrid RANS-LES strategy intended for application to turbulent separated flow problems has been developed. The methodology couples the standard RANS k-ε linear eddy-viscosity turbulence model with a two-equation nonlinear SGS model for LES. The nonlinear SGS model, inspired by the triple model idea of Bardina et al. [5], replaces the scale-similarity term of the original triple model, which is not Galilean invariant, with the modified Leonard stress tensor, which is Galilean invariant. The SGS model also contains two nonlinear and Galilean invariant terms based on the products of the strain-rate and rotation-rate tensors for an improved representation of the forward and backward scatter of energy between the resolved and unresolved scales and the anisotropy effects. Furthermore, the model formulation does not use a characteristic length scale for any of its terms and hence naturally avoids the ambiguities associated with defining a proper length scale for anisotropic grids. The nonlinear SGS model additionally requires the solutions of two transport equations for the subgrid turbulent kinetic energy and the subgrid viscous dissipation, which have the same structural form as the transport equations of the standard RANS k-ε model. Hence, the two transport equations for the total/subgrid turbulent kinetic energy and the total/subgrid viscous dissipation are solved in the entire domain with the coefficients of the production and destruction terms in the total/subgrid viscous dissipation transport equation set differently between the two zones. A source term is additionally included in the total viscous dissipation transport equation solved in the RANS zone and serves as a correction mechanism when the logarithmic-layer compatibility condition is not strictly satisfied among the RANS model coefficients. The coupling between the RANS and LES zones is accomplished by means of a smooth blending function that linearly combines the RANS and SGS turbulent stresses. A similar blending is also applied to the production, destruction and turbulent diffusion terms of the two transport equations. The blending function depends only on the wall-normal distance and the local maximum grid spacing. The hybrid method applies the RANS calculation in the near-wall region and switches to the LES in the outer region; hence, it can be considered an alternative form of a WMLES.

Application of the proposed HRLES methodology to two benchmark smooth-body flow separation problems has been demonstrated. Both test cases feature flow separation induced by a strong APG that, in turn, is generated due to a change in the body contour. The analysis of the results show that the main features of both problems are captured with a reasonable level of accuracy at about three orders of magnitude lower computational cost relative to that of DNS. More specifically, the grid point ratio between the DNS and the HRLES is $10.2 \times 10^9/29 \times 10^6 \approx 352$ for the speed-bump flow and $10.3 \times 10^9/23.6 \times 10^6 \approx 436$ for the smooth-ramp flow. The time step of the HRLES is six times the value taken in the DNS in both test cases while the computational cost of the HRLES per time step per grid point is about 2.5 times that of the DNS. This additional cost comes from having to solve the two transport equations as well as the dynamic determination of the nonlinear SGS model coefficients that require filtering operations on a number of quantities and the additional subiteration(s) of the implicit time integration scheme needed at high CFL numbers. Hence, for a given convective time unit worth of simulation time, the computational cost ratio between the DNS and the HRLES is $352 \times 6/2.5 \approx 845$ for the speed-bump flow and $436 \times 6/2.5 \approx 1046$ for the smooth-ramp flow. Analysis of the results also demonstrated that the present approach is free of the logarithmic-layer mismatch encountered in some other hybrid approaches as well as the modeled-stress depletion that may occur in DES under certain circumstances. However, the underprediction of skin friction within the recovery region in both test cases remains a matter that warrants further investigation. As the accuracy of the near-wall solution strongly depends on the performance of the RANS turbulence model, rectification of this matter would likely require some enhancements to the model, which could be in the form of a near-wall source term that can become active/inactive in particular regions of the flowfield based on some local features.

Acknowledgments

This work was sponsored by the NASA Transformational Tools and Technologies Project of the Transformative Aeronautics Concepts Program under the Aeronautics Research Mission Directorate. The work of the first author was sponsored by NASA under Contract No. 80LARC23DA003. The calculations were made possible by the computing resources provided by the NASA High-End Computing Program through the NASA Advanced Supercomputing Division at Ames Research Center.

References

[1] K. Abe. A hybrid LES/RANS approach using an anisotropy-resolving algebraic turbulence model. *International Journal of Heat and Fluid Flow*, 26(2):204–222, April 2005. `doi:10.1016/j.ijheatfluidflow.2004.08.009`.

[2] K. Abe. An improved anisotropy-resolving subgrid-scale model with the aid of a scale-similarity modeling concept. *International Journal of Heat and Fluid Flow*, 39:42–52, February 2013. `doi:10.1016/j.ijheatfluidflow.2012.12.001`.

[3] R. Agrawal, S. T. Bose, and P. Moin. Nonequilibrium wall model for large eddy simulations of complex flows exhibiting turbulent smooth body separation. *Physical Review Fluids*, 9(12):124603, December 2024. `doi:10.1103/PhysRevFluids.9.124603`.

[4] G. Ashcroft and X. Zhang. Optimized prefactored compact schemes. *Journal of Computational Physics*, 190(2):459–477, September 2003. `doi:10.1016/S0021-9991(03)00293-6`.

[5] J. Bardina, J. H. Ferziger, and W. C. Reynolds. Improved turbulence models based on large eddy simulation of homogeneous, incompressible, turbulent flows. Report No. TF-19, Thermosciences Division, Department of Mechanical Engineering, Stanford University, Stanford, CA, May 1983.

[6] S. T. Bose and G. I. Park. Wall-modeled large-eddy simulation of complex turbulent flows. *Annual Review of Fluid Mechanics*, 50:535–561, January 2018. doi:10.1146/annurev-fluid-122316-045241.

[7] B. Chaouat and R. Schiestel. A new partially integrated transport model for subgrid-scale stresses and dissipation rate for turbulent developing flows. *Physics of Fluids*, 17(6):065106, June 2005. doi:10.1063/1.1928607.

[8] K.-Y. Chien. Predictions of channel and boundary-layer flows with a low-Reynolds-number turbulence model. *AIAA Journal*, 20(1):33–38, January 1982. doi:10.2514/3.51043.

[9] J. W. Deardorff. The use of subgrid transport equations in a three-dimensional model of atmospheric turbulence. *Journal of Fluids Engineering*, 95(3):429–438, September 1973. doi:10.1115/1.3447047.

[10] P. A. Durbin. Turbulence closure modeling near rigid boundaries. Annual Research Briefs 1990, Center for Turbulence Research, Stanford University, California, CA, February 1991.

[11] P. A. Durbin. Application of a near-wall turbulence model to boundary layers and heat transfer. *International Journal of Heat and Fluid Flow*, 14(4):316–323, December 1993. doi:10.1016/0142-727X(93)90004-7.

[12] J. A. Ekaterinaris. Implicit, high-resolution, compact schemes for gas dynamics and aeroacoustics. *Journal of Computational Physics*, 156(2):272–299, December 1999. doi:10.1006/jcph.1999.6360.

[13] S. Fan, B. Lakshminarayana, and M. Barnett. Low-Reynolds-number k-ε model for unsteady turbulent boundary-layer flows. *AIAA Journal*, 31(10):1777–1784, October 1993. doi:10.2514/3.11849.

[14] A. Favre. Turbulence: Space-time statistical properties and behavior in supersonic flows. *Physics of Fluids*, 26(10):2851–2863, October 1983. doi:10.1063/1.864049.

[15] J. Fröhlich and D. von Terzi. Hybrid LES/RANS methods for the simulation of turbulent flows. *Progress in Aerospace Sciences*, 44(5):349–377, July 2008. doi:10.1016/j.paerosci.2008.05.001.

[16] D. V. Gaitonde and M. R. Visbal. Padé-type higher-order boundary filters for the Navier-Stokes equations. *AIAA Journal*, 38(11):2103–2112, November 2000. doi:10.2514/2.872.

[17] F. Gallerano, E. Pasero, and G. Cannata. A dynamic two-equation sub grid scale model. *Continuum Mechanics and Thermodynamics*, 17(2):101–123, May 2005. doi:10.1007/s00161-004-0190-4.

[18] M. Germano. A proposal for a redefinition of the turbulent stresses in the filtered Navier-Stokes equations. *Physics of Fluids*, 29(7):2323–2324, July 1986. doi:10.1063/1.865568.

[19] M. Germano, U. Piomelli, P. Moin, and W. H. Cabot. A dynamic subgrid-scale eddy viscosity model. *Physics of Fluids A: Fluid Dynamics*, 3:1760–1765, July 1991. doi:10.1063/1.857955.

[20] S. S. Girimaji. Partially-averaged Navier-Stokes model for turbulence: A Reynolds-averaged Navier-Stokes to direct numerical simulation bridging method. *Journal of Applied Mechanics*, 73(3):413–421, May 2006. doi:10.1115/1.2151207.

[21] C. M. Hrenya, E. J. Bolio, D. Chakrabarti, and J. L. Sinclair. Comparison of low Reynolds number $k-\varepsilon$ turbulence models in predicting fully developed pipe flow. *Chemical Engineering Science*, 50(12):1923–1941, June 1995. doi:10.1016/0009-2509(95)00035-4.

[22] W. P. Jones and B. E. Launder. The prediction of laminarization with a two-equation model of turbulence. *International Journal of Heat and Mass Transfer*, 15(2):301–314, February 1972. doi:10.1016/0017-9310(72)90076-2.

[23] W. P. Jones and B. E. Launder. The calculation of low-Reynolds-number phenomena with a two-equation model of turbulence. *International Journal of Heat and Mass Transfer*, 16(6):1119–1130, June 1973. doi:10.1016/0017-9310(73)90125-7.

[24] R. Kamogawa, Y. Tamaki, and S. Kawai. Ordinary-differential-equation-based nonequilibrium wall modeling for large-eddy simulation. *Physical Review Fluids*, 8:064605, June 2023. doi:10.1103/PhysRevFluids.8.064605.

[25] W.-W. Kim and S. Menon. Application of the localized dynamic subgrid-scale model to turbulent wall-bounded flows. AIAA Paper 97-0210, 35th Aerospace Sciences Meeting and Exhibit, Reno, NV, January 1997. doi:10.2514/6.1997-210.

[26] J. Larsson, S. Kawai, J. Bodart, and I. Bermejo-Moreno. Large eddy simulation with modeled wall-stress: Recent progress and future directions. *Mechanical Engineering Reviews*, 3(1):15–00418, January 2016. doi:10.1299/mer.15-00418.

[27] B. E. Launder and D. B. Spalding. The numerical computation of turbulent flows. *Computer Methods in Applied Mechanics and Engineering*, 3(2):269–289, March 1974. doi:10.1016/0045-7825(74)90029-2.

[28] S. K. Lele. Compact finite difference schemes with spectral-like resolution. *Journal of Computational Physics*, 103(1):16–42, November 1992. doi:10.1016/0021-9991(92)90324-R.

[29] D. K. Lilly. A proposed modification of the Germano subgrid-scale closure method. *Physics of Fluids A: Fluid Dynamics*, 4(3):633–635, March 1992. doi:10.1063/1.858280.

[30] C. Meneveau and J. Katz. Scale-invariance and turbulence models for large-eddy simulation. *Annual Review of Fluid Mechanics*, 32(1):1–32, January 2000. doi:10.1146/annurev.fluid.32.1.1.

[31] F. R. Menter. Improved two-equation $k-\omega$ turbulence models for aerodynamic flows. NASA Technical Memorandum 103975, October 1992.

[32] F. R. Menter. Two-equation eddy-viscosity turbulence models for engineering applications. *AIAA Journal*, 32(8):1598–1605, August 1994. doi:10.2514/3.12149.

[33] F. R. Menter and M. Kuntz. Adaptation of eddy-viscosity turbulence models to unsteady separated flow behind vehicles. In *The Aerodynamics of Heavy Vehicles: Trucks, Buses, and Trains. Lecture Notes in Applied and Computational Mechanics, Vol. 19*, pages 339–352. Springer, Berlin, Heidelberg, 2004. doi:10.1007/978-3-540-44419-0_30.

[34] B. Merci, C. De Langhe, E. Dick, and L. J. Vierendeels. Heat transfer in turbulent impinging jets with a non-linear k-ε model. *WIT Transactions on Engineering Sciences*, 36:651–660, 2002.

[35] B. Merci, C. De Langhe, L. J. Vierendeels, and E. Dick. A quasi-realizable cubic low-Reynolds eddy-viscosity turbulence model with a new dissipation rate equation. *Flow, Turbulence and Combustion*, 66(2):133–157, March 2001. doi:10.1023/A:1017955003995.

[36] R. Mokhtarpoor and S. Heinz. Dynamic large eddy simulation: Stability via realizability. *Physics of Fluids*, 29(10):105104, October 2017. doi:10.1063/1.4986890.

[37] N. V. Nikitin, F. Nicoud, B. Wasistho, K. D. Squires, and P. R. Spalart. An approach to wall modeling in large-eddy simulations. *Physics of Fluids*, 12(7):1629–1632, July 2000. doi:10.1063/1.870414.

[38] A. Parente, C. Gorlé, J. van Beeck, and C. Benocci. Improved $k-\varepsilon$ model and wall function formulation for the RANS simulation of ABL flows. *Journal of Wind Engineering and Industrial Aerodynamics*, 99(4):267–278, April 2011. doi:10.1016/j.jweia.2010.12.017.

[39] G. I. Park and P. Moin. An improved dynamic non-equilibrium wall-model for large eddy simulation. *Physics of Fluids*, 26(1):015108, January 2014. doi:10.1063/1.4861069.

[40] V. C. Patel, W. Rodi, and G. Scheuerer. Turbulence models for near-wall and low Reynolds number flows: A review. *AIAA Journal*, 23(9):1308–1319, September 1985. doi:10.2514/3.9086.

[41] J. B. Perot and J. Gadebusch. A self-adapting turbulence model for flow simulation at any mesh resolution. *Physics of Fluids*, 19(11):115105, November 2007. doi:10.1063/1.2780195.

[42] J. B. Perot and J. Gadebusch. A stress transport equation model for simulating turbulence at any mesh resolution. *Theoretical and Computational Fluid Dynamics*, 23(4):271–286, June 2009. doi:10.1007/s00162-009-0113-x.

[43] U. Piomelli and E. Balaras. Wall-layer models for large eddy simulations. *Annual Review of Fluid Mechanics*, 34:349–374, January 2002. doi:10.1146/annurev.fluid.34.082901.144919.

[44] M. Pontiggia, M. Derudi, V. Busini, and R. Rota. Hazardous gas dispersion: A CFD model accounting for atmospheric stability classes. *Journal of Hazardous Materials*, 171(1–3):739–747, November 2009. doi:10.1016/j.jhazmat.2009.06.064.

[45] M. M. Rahman and T. Siikonen. Near-wall turbulence modelling with enhanced dissipation. *International Journal for Numerical Methods in Fluids*, 42(9):979–997, July 2003. doi:10.1002/fld.569.

[46] M. M. Rahman and T. Siikonen. Low Reynolds number k-ε model for near-wall flow. *International Journal for Numerical Methods in Fluids*, 47(4):325–338, February 2005. doi:10.1002/fld.809.

[47] P. J. Richards and R. P. Hoxey. Appropriate boundary conditions for computational wind engineering models using the $k-\varepsilon$ turbulence model. *Journal of Wind Engineering and Industrial Aerodynamics*, 46–47:145–153, August 1993. doi:10.1016/0167-6105(93)90124-7.

[48] R. Schiestel and A. Dejoan. Towards a new partially integrated transport model for coarse grid and unsteady turbulent flow simulations. *Theoretical and Computational Fluid Dynamics*, 18(6):443–468, February 2005. doi:10.1007/s00162-004-0155-z.

[49] P. Schlatter and R. Örlü. Assessment of direct numerical simulation data of turbulent boundary layers. *Journal of Fluid Mechanics*, 659:116–126, September 2010. doi:10.1017/S0022112010003113.

[50] J.-E. Schumann, S. Toosi, and J. Larsson. Assessment of grid anisotropy effects on large-eddy-simulation models with different length scales. *AIAA Journal*, 58(10):4522–4533, October 2020. doi:10.2514/1.J059576.

[51] U. Schumann. Subgrid scale model for finite difference simulations of turbulent flows in plane channels and annuli. *Journal of Computational Physics*, 18(4):376–404, August 1975. doi:10.1016/0021-9991(75)90093-5.

[52] K. B. Shah. *Large eddy simulations of flow past a cubic obstacle*. PhD thesis, Department of Mechanical Engineering, Stanford University, Stanford, CA, June 1998.

[53] M. L. Shur, P. R. Spalart, M. Kh. Strelets, and A. K. Travin. A hybrid RANS-LES approach with delayed-DES and wall-modelled LES capabilities. *International Journal of Heat and Fluid Flow*, 29(6):1638–1649, December 2008. doi:10.1016/j.ijheatfluidflow.2008.07.001.

[54] P. R. Spalart. Detached-eddy simulation. *Annual Review of Fluid Mechanics*, 41:181–202, January 2009. doi:10.1146/annurev.fluid.010908.165130.

[55] P. R. Spalart, S. Deck, M. L. Shur, K. D. Squires, M. Kh. Strelets, and A. K. Travin. A new version of detached-eddy simulation, resistant to ambiguous grid densities. *Theoretical and Computational Fluid Dynamics*, 20(3):181–195, July 2006. doi:10.1007/s00162-006-0015-0.

[56] P. R. Spalart and A. V. Garbaruk. Correction to the Spalart-Allmaras turbulence model, providing more accurate skin friction. *AIAA Journal*, 58(5):1903–1905, April 2020. doi:10.2514/1.J059489.

[57] A. Uzun and M. Y. Hussaini. Investigation of high frequency noise generation in the near-nozzle region of a jet using large eddy simulation. *Theoretical and Computational Fluid Dynamics*, 21(4):291–321, July 2007. doi:10.1007/s00162-007-0048-z.

[58] A. Uzun and M. Y. Hussaini. Simulation of noise generation in near-nozzle region of a chevron nozzle jet. *AIAA Journal*, 47(8):1793–1810, August 2009. doi:10.2514/1.36659.

[59] A. Uzun and M. Y. Hussaini. Prediction of noise generated by a round nozzle jet flow using computational aeroacoustics. *Journal of Computational Acoustics*, 19(3):291–316, September 2011. doi:10.1142/S0218396X11004365.

[60] A. Uzun, M. Y. Hussaini, and C. L. Streett. Large-eddy simulation of a wing tip vortex on overset grids. *AIAA Journal*, 44(6):1229–1242, June 2006. doi:10.2514/1.17999.

[61] A. Uzun and M. R. Malik. Effect of spatial filtering in implicit large-eddy simulations of separated flows. *AIAA Journal*, 57(12):5575–5581, December 2019. doi:10.2514/1.J058382.

[62] A. Uzun and M. R. Malik. Wall-resolved large-eddy simulations of transonic shock-induced flow separation. *AIAA Journal*, 57(5):1955–1972, May 2019. doi:10.2514/1.J057850.

[63] A. Uzun and M. R. Malik. Simulation of a turbulent flow subjected to favorable and adverse pressure gradients. *Theoretical and Computational Fluid Dynamics*, 35(3):293–329, June 2021. doi:10.1007/s00162-020-00558-4.

[64] A. Uzun and M. R. Malik. A dynamic nonlinear subgrid-scale model for large-eddy simulation of complex turbulent flows. NASA Technical Memorandum 20220013891, October 2022.

[65] A. Uzun and M. R. Malik. High-fidelity simulation of turbulent flow past Gaussian bump. *AIAA Journal*, 60(4):2130–2149, April 2022. doi:10.2514/1.J060760.

[66] A. Uzun and M. R. Malik. Direct numerical simulation of smooth-body flow separation around a ramp. *Computers & Fluids*, 301:106779, October 2025. doi:10.1016/j.compfluid.2025.106779.

[67] M. R. Visbal and D. V. Gaitonde. Very high-order spatially implicit schemes for computational acoustics on curvilinear meshes. *Journal of Computational Acoustics*, 9(4):1259–1286, December 2001. doi:10.1016/S0218-396X(01)00054-1.

[68] B. Vreman, B. Geurts, and H. Kuerten. Realizability conditions for the turbulent stress tensor in large-eddy simulation. *Journal of Fluid Mechanics*, 278:351–362, November 1994. doi:10.1017/S0022112094003745.

[69] J. J. Wagner, W. K. Anderson, L. Wang, and V. N. Vatsa. A simple DDES shielding technique to mitigate modeled-stress depletion and promote rapid RANS-to-LES transition. AIAA Paper 2026-0523, AIAA SciTech 2026 Forum, Orlando, FL, January 2026. doi:10.2514/6.2026-0523.

[70] Z. Yang and T. H. Shih. New time scale based $k-\varepsilon$ model for near-wall turbulence. *AIAA Journal*, 31(7):1191–1198, July 1993. doi:10.2514/3.11752.